



Estimation of the Paris NO_x emissions from mobile MAX-DOAS observations and CHIMERE model simulations during the MEGAPOLI campaign using the closed integral method

Reza Shaiganfar¹, Steffen Beirle¹, Hugo Denier van der Gon², Sander Jonkers², Jeroen Kuenen², Herve Petetin³, Qijie Zhang³, Matthias Beekmann³, and Thomas Wagner¹

¹Max Planck Institute for Chemistry, Mainz, Germany

²TNO, Climate, Air and Sustainability, Utrecht, the Netherlands

³LISA/IPSL, UMR CNRS 7583, Université Paris Est Créteil et Université Paris Diderot, Créteil, France

Correspondence to: Thomas Wagner (thomas.wagner@mpic.de)

Received: 13 October 2016 – Discussion started: 14 November 2016

Revised: 14 November 2016 – Accepted: 24 May 2017 – Published: 29 June 2017

Abstract. We determined NO_x emissions from Paris in summer 2009 and winter 2009/2010 by applying the closed integral method (CIM) to a large set of car multi-axis differential optical absorption spectroscopy (MAX-DOAS) measurements performed within the framework of the MEGAPOLI project (<http://megapoli.dmi.dk/>). MAX-DOAS measurements of the tropospheric NO₂ vertical column density (VCD) were performed in large circles around Paris. From the combination of the observed NO₂ VCDs with wind fields, the NO₂ influx into and the outflux from the encircled area was determined. The difference between the influx and outflux represents the total emission. Compared to previous applications of the CIM, the large number of measurements during the MEGAPOLI campaign allowed the investigation of important aspects of the CIM. In particular, the applicability of the CIM under various atmospheric conditions could be tested. Another important advantage of the measurements during MEGAPOLI is that simultaneous atmospheric model simulations with a high spatial resolution ($3 \times 3 \text{ km}^2$) are available for all days. Based on these model data, it was possible to test the consistency of the CIM and to derive information about favourable or non-favourable conditions for the application of the CIM. We found that in most situations the uncertainties and the variability in the wind data dominate the total error budget, which typically ranges between 30 and 50%. Also, measurement gaps and uncertainties in the partitioning ratio between NO and NO₂ are important error sources. Based on a consistency check,

we deduced a set of criteria on whether measurement conditions are suitable or not for the application of the CIM. We also developed a method for the calculation of the total error budget of the derived NO_x emissions. Typical errors are between ± 30 and $\pm 50\%$ for individual days (with one full circle around Paris). From the application of the CIM to car MAX-DOAS observations we derive daily average NO_x emissions for Paris of $4.0 \times 10^{25} \text{ molec s}^{-1}$ for summer and of $6.9 \times 10^{25} \text{ molec s}^{-1}$ in winter. These values are a factor of about 1.4 and 2.0 larger than the corresponding emissions derived from the application of the CIM to the model data, using the Toegepast Natuurwetenschappelijk Onderzoek (TNO) MEGAPOLI emission inventory, in summer and winter, respectively. Similar ratios (1.5 and 2.3 for summer and winter, respectively) were found for the comparison with the Monitoring Atmospheric composition and climate III (MACC-III) emission inventory. The highest NO_x emissions were found during some cold days in February. Enhanced domestic heating and a reduced conversion efficiency of catalytic converters might contribute to these enhanced NO_x emissions.

1 Introduction

Emission estimates of atmospheric trace species are important as input for model simulations and for the quantification of air pollution. Such emissions can be quantified using bottom-up or top-down techniques. Here, we apply a “local” top-down approach, the closed integral method (CIM), based on car multi-axis differential optical absorption spectroscopy (MAX-DOAS) measurements in combination with wind information. For the quantification of emissions, car MAX-DOAS measurements are performed in large circles around large cities or other strong emissions sources (Rivera et al., 2009; Ibrahim et al., 2010; Wagner et al., 2010; Shaiganfar et al., 2011, 2015). In contrast to top-down approaches based on satellite observations (e.g. Ghude et al., 2013 and references therein), emission estimates based on car MAX-DOAS measurements are independent of model simulations. They also depend much less on assumptions about the atmospheric lifetimes. Moreover, car MAX-DOAS measurements are much less affected by clouds and aerosols than satellite observations.

Our study focusses on car MAX-DOAS observations during two extended measurement campaigns in Paris (Shaiganfar et al., 2015) within the framework of the European project Megacities: Emissions, urban, regional and Global Atmospheric POLLution and climate effects, and Integrated tools for assessment and mitigation (MEGAPOLI; Baklanov et al., 2011; Beekmann et al., 2015; see also <http://megapoli.dmi.dk/>). During the first campaign, in summer 2009, NO_x emissions could be quantified on 9 days. During the second campaign, in winter 2009/2010, NO_x emissions could be quantified on 22 days. Another important aspect of this study is that highly resolved ($3 \times 3 \text{ km}^2$) model simulations were available for all days of the car MAX-DOAS measurements. Thus, compared to previous studies, which are based on only a few days of car MAX-DOAS observations, the comprehensive set of car MAX-DOAS observations during both MEGAPOLI campaigns is well suited to address several important questions.

- What are the uncertainties in NO_x emission estimates based on the application of the CIM to car MAX-DOAS observations?
- Which measurement settings (e.g. driving route) and conditions (e.g. wind speed and direction) are favourable, and which should be avoided?
- How can the method be improved further?
- How representative are the derived emissions of a specific time of day or of the daily average?
- What are the total NO_x emissions from Paris during either summer or winter? How consistent are they with existing emission inventories?

The paper is organised as follows: in Sect. 2 both MEGAPOLI campaigns and the car MAX-DOAS measurements are introduced. Section 3 gives an overview of the CHIMERE model. In Sect. 4 the different steps of our approach are described in detail and the associated errors are discussed and quantified. Section 5 describes a consistency check of the method based on model simulations, and gives an overview on the derived NO_x emissions for Paris during both campaigns. A summary and conclusions are provided in Sect. 7.

2 MEGAPOLI campaigns and car MAX-DOAS measurements

The car MAX-DOAS observations in and around Paris were described in detail in Shaiganfar et al. (2015). Here, we give only a brief overview. Two extensive measurement campaigns were organised within the framework of the MEGAPOLI project (Baklanov et al., 2011; see also <http://megapoli.dmi.dk/>) in June and July 2009 and in January and February 2010. Car MAX-DOAS measurements were performed on 25 days in summer and 29 days in winter. One major aim of the car MAX-DOAS measurements was to quantify the total NO_x emissions from Paris. For that purpose we applied the CIM by carrying out car MAX-DOAS measurements of the tropospheric vertical column density (VCD) along closed circles around Paris. Details on the data analysis of the car MAX-DOAS measurements are given in Shaiganfar et al. (2015), who used the same data set for comparison with satellite and model data.

On some days, the driving routes were not well suited for the determination of NO_x emissions because the driving routes did not cover full circles and/or the circles were too small (they covered only the city centre). On 9 days in summer 2009 and 22 days in winter 2009/2010, meaningful emission estimates were possible. In Fig. 1, a measurement example for 12 February 2010 is shown. This example represents almost ideal conditions because the measurements were performed around a rather large circle without major gaps. Also, as indicated by the arrows, the near-surface wind speed (for details, see Sect 4.1) was rather high (about 8.5 m s^{-1}) and the wind speed and wind direction did not change strongly during the period of the measurements. The transport of polluted air masses towards the south-west is indicated by the enhanced NO₂ VCDs observed at the lower left part of the circle.

3 CHIMERE model simulations

The CHIMERE chemical transport model (CTM; Schmidt et al., 2001; Menut et al., 2012, 2013) (www.lmd.polytechnique.fr/chimere) has been developed since 1997 by IPSL (Institut Pierre Simon Laplace) and INERIS (Institut National de l'Environnement Industriel et des Risques).

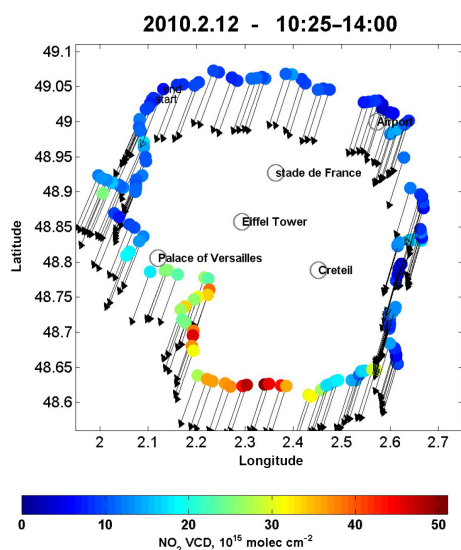


Figure 1. Tropospheric vertical column densities (VCDs) of NO₂ derived from car MAX-DOAS measurements around Paris on 12 February 2010 (each dot indicates an individual measurement). The arrows indicate wind speed and direction taken from the regional CHIMERE model. The average wind speed was about 8.5 m s⁻¹.

Simulations are performed with a horizontal resolution of 3 × 3 km² and a vertical discretisation comprising eight vertical layers from the ground to about 5 km, with decreasing vertical resolution with altitude. The Toegest Naturowetenschappelijk Onderzoek (TNO) MEGAPOLI inventory (Denier van der Gon et al., 2011; Timmermans et al., 2013) for the Paris region is a combination of a regional European emission inventory and a local emission inventory for Paris made by Airparif (2010), the city's air quality and emission inventory authority. The base year of both inventories is 2005. In the TNO-MEGAPOLI inventory, the year 2005 emissions for Paris (Île-de-France) have been replaced with those from Airparif for the same year. The NO_x emissions by month and by source sector are shown in Fig. 2a. Traffic is the largest NO_x source in Paris. NO_x emissions in winter are about 20 % larger than in summer due to the seasonal cycle of residential, commercial and other combustion processes.

An example of the spatial distribution and the diurnal variation in the NO_x emissions over Paris is shown in Fig. 2b and c. The location and emission strength of the most important point sources are presented in Table 1. It should be noted that since the replacement of Paris emissions with the Île-de-France inventory from Airparif causes a change in the total emissions for France, the national total emissions would no longer be consistent with the official reported emissions. Therefore, the difference in emissions has been attributed to the whole country except for the Île-de-France region (per pollutant and emission source category). For the Paris region the emission data are available at 1 km resolution, but for

Table 1. Location and type of major point sources in the domain of study.

Long	Lat	Type	NO _x emissions (Mg yr ⁻¹)
1.769325	48.96941	Power plant	3254
2.410617	48.79099	Power plant	3088
2.938827	48.59174	Refinery	1078
2.705922	48.23307	Industry	871
2.328981	48.90785	Power plant	869
2.979367	48.58253	Refinery	710
1.810182	48.97858	Industry	632

the CHIMERE simulations they were summed up to the spatial resolution of the model (3 km). Meteorological data are produced at hourly time steps with the Pennsylvania State University (PSU)/NCAR Mesoscale Model (MM5; Dudhia et al., 1993) (see Fig. 3). More information about the specific CHIMERE simulations during MEGAPOLI can be found in Zhang et al. (2013, 2015), Petetin et al. (2015) and Shaiganfar et al. (2015).

4 Determination of the NO_x emissions

4.1 Calculation of the NO₂ fluxes

The NO_x flux from the encircled area was calculated in several steps. In the first step the NO₂ fluxes were integrated using the CIM.

$$F_{\text{NO}_2} = \oint_s \text{VCD}(s) \cdot \boldsymbol{\omega} \cdot \boldsymbol{n} \cdot ds \quad (1)$$

Here, VCD indicates the tropospheric vertical column density of NO₂ (the vertically integrated NO₂ concentration), $\boldsymbol{\omega}$ indicates the wind vector and \boldsymbol{n} the unit vector orthogonal to the driving route. Since individual MAX-DOAS measurements were performed for limited periods of time (about 1 min), the integral is substituted by a sum over the fluxes calculated for the segments corresponding to individual measurements:

$$F_{\text{NO}_2} \approx \sum_i \text{VCD}_i \cdot \omega_i \cdot \sin(\beta_i) \cdot \Delta s_i \quad (2)$$

Here, VCD_{*i*} represents the NO₂ VCD obtained from measurement *i*; ω_i represents the average wind speed during the period of the car MAX-DOAS measurements. β_i represents the angle between the (average) wind direction and the driving direction at the location of measurement *i*; Δs_i indicates the distance between the location of measurement *i* and *i* + 1.

As wind data we used the wind fields from the model simulations at different heights (see Sect. 3 and Fig. 3). From this

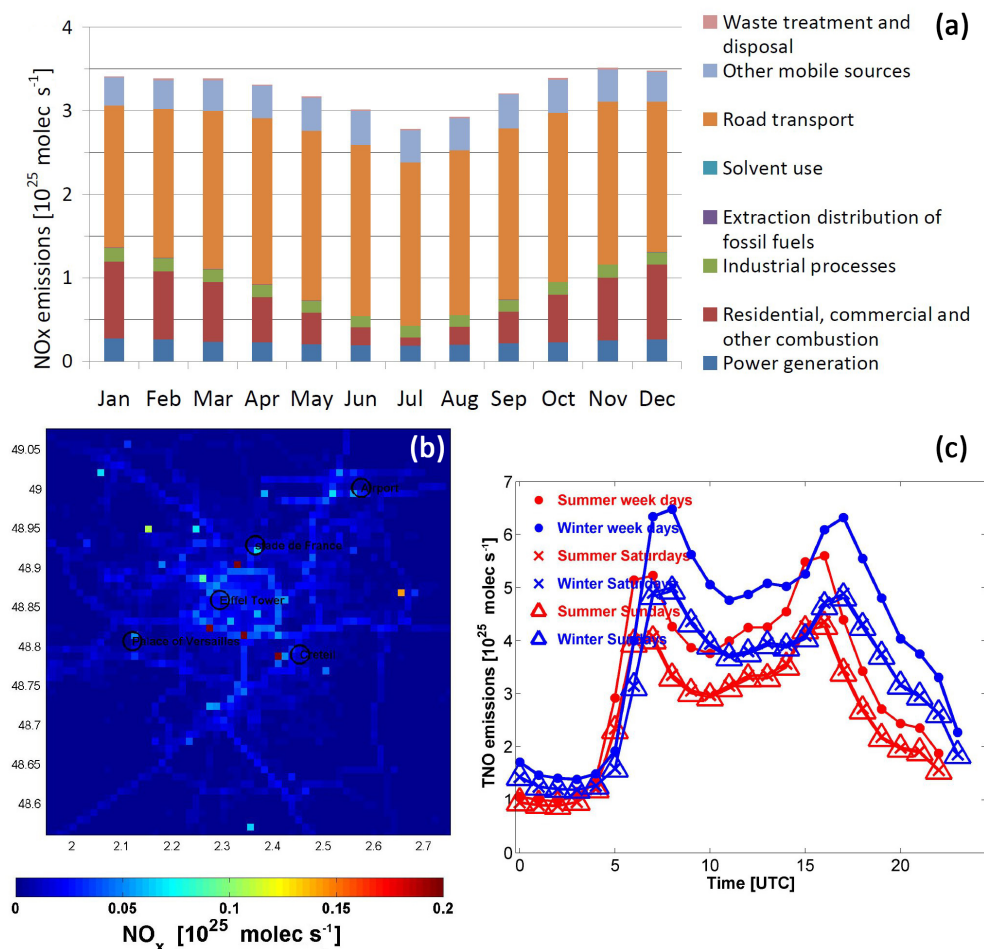


Figure 2. (a) Seasonal cycle of the NO_x emissions for the greater Paris area (Île-de-France) in 2009 by source sector per month. Examples of the spatial distribution (b) and the diurnal variation (c) of the integrated NO_x emissions over the area shown in (b). For the Paris region the emission data are available at 1 km resolution, but for the CHIMERE simulations they were summed up to the spatial resolution of the model (3 km) (Airparif, 2010).

data set we calculated the average wind speed and direction for all individual locations and times of the car MAX-DOAS measurements along the circle (for the vertical averaging, see below). These averaged wind data were chosen (instead of using spatio-temporally resolved wind data) because usually 3-D high-resolution wind fields are not available for the locations of the car MAX-DOAS measurements. The effect of the use of spatio-temporally resolved wind data (interpolated in time and space to the individual car MAX-DOAS observations) is usually small (except for days with high wind variability). It is investigated in detail in Sect. 4.6.3.

As an example, wind data for 24 January 2010 are shown in Fig. 3. On this day rather large variations in the wind speed and direction were found during the period of the car MAX-DOAS measurements: the wind speed at the surface varied by about a factor of 2; the wind direction at the surface changed by about 20°. For most days smaller variations in both quantities are found.

Both wind speed and direction vary systematically with altitude (see, e.g., Fig. 3). Thus, a choice has to be made regarding the question in which altitude range most NO_x is probably situated because the wind data for this altitude range determine the NO_x flux. Since our measurements were performed close to the NO_x emission sources and since most NO_x emission sources are located close to the surface, we assume exponentially decreasing NO_x concentration profiles with scale heights of 300 m (winter) and 500 m (summer). We averaged the wind data from the PSU/NCAR Mesoscale Model (MM5; Dudhia et al., 1993) between the surface and 1000 m altitude weighted by these exponentially decreasing profiles.

$$\omega_{\text{avg}} = \frac{\sum_i \omega(z_i) \cdot e^{-\frac{z_i}{z_0}}}{\sum_i e^{-\frac{z_i}{z_0}}} \quad (3)$$

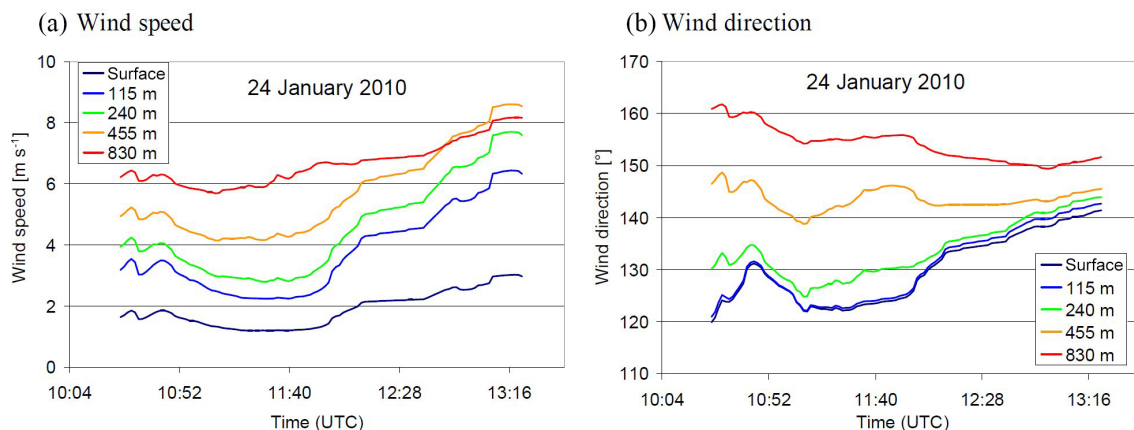


Figure 3. Wind speed (a) and direction with respect to north (b) at different altitudes for 24 January 2010 obtained from the MM5 model during the time of measurement of the entire single circle.

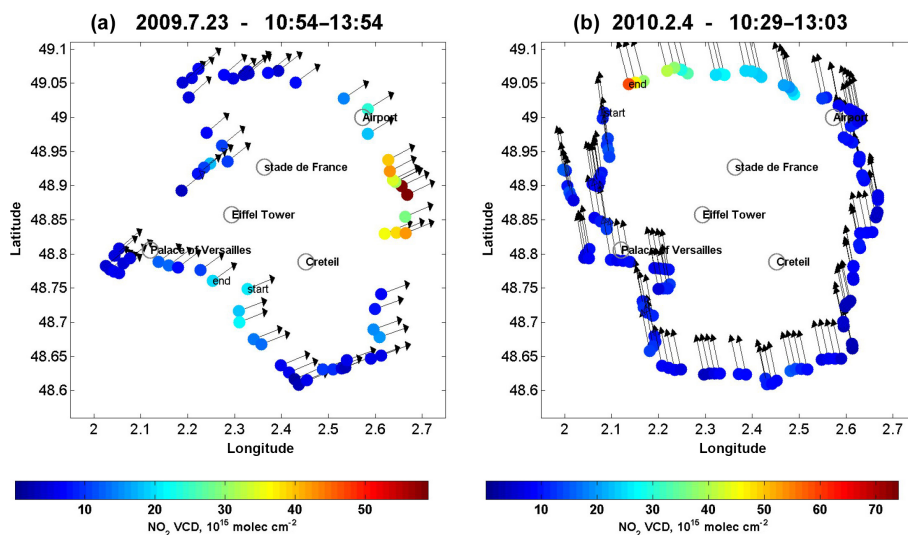


Figure 4. Car MAX-DOAS results for 23 July 2009 (a) and 4 February (b). On 23 July 2009 several gaps due to instrumental problems occurred. On 4 February, no obvious gap is seen, but a large difference in the NO₂ VCDs between the start and end of the circle is found.

Here, $\omega(z_i)$ indicates the wind vector at altitude z_i (see Fig. 3) and z_0 indicates the assumed scale height of 300 and 500 m for summer and winter, respectively. The chosen vertical NO_x concentration profiles are rough estimates for the trace gas profiles close to emission sources and take into account the effect of different vertical mixing conditions and atmospheric lifetimes in different seasons. On individual days, however, substantial deviations from these assumptions can also be found (see Fig. A2 in the Appendix). Nevertheless, changes in the wind fields with altitude are typically smaller at higher altitudes. Thus, the effect of the assumed profile height has a rather small influence on the derived wind fields. The effect of uncertainties in the wind speed and direction is discussed in Sect. 4.6.3. We also compared the wind fields from the MM5 model with wind profiles measured by a cube lidar at the Site Instrumental de Recherche par Télédétection

Atmosphérique (SIRTA) site at Palaiseu in the south-west of Paris (Haeffelin et al., 2005). The comparison was possible for three altitude layers between 40 and 200 m. We compared the averaged wind speed and wind directions during the periods of the MAX-DOAS measurements (see Fig. A1). For the layers at 120 and 200 m, almost perfect agreement is found between both data sets. However, for the surface layer the model data systematically underestimate the wind speed obtained by the lidar. We have no clear explanation for these differences, but probably they are related to the limited horizontal resolution of the model data. Fortunately, the differences in the wind speed become much smaller (typically $< 0.3 \text{ m s}^{-1}$) when weighted with the exponential NO_x profiles with scale heights of 300 and 500 m, respectively. Here, it should also be noted that the exact choice of the scale height is not critical: changes in the scale heights be-

tween 200 and 700 m usually lead to differences in the wind speed $< 0.5 \text{ m s}^{-1}$ and wind direction $< 5^\circ$. The errors in the derived NO_x emissions associated with uncertainties in the wind speed and direction are quantified in Sect. 4.6.3.

4.2 Effect of measurement gaps along the circles

Measurement gaps can occur due to various reasons. Besides missing spectra due to instrumental problems, the quality of some measured spectra might also not be good enough for a meaningful data analysis (e.g. due to over- or undersaturation caused by obstacles like trees, bridges or tunnels). In Fig. 4a measurements for 23 July 2009 are shown. On this day several gaps are present. The effect of gaps on the emission estimates can be particularly large if strong gradients of the trace gas concentrations are present. This is the case for, e.g., some of the gaps shown in Fig. 4a as indicated by different NO₂ VCDs on both sides of the gap (e.g. on the eastern side of the circle). Here, it is important to note that even if similar NO₂ VCDs are measured on both sides of a gap (like on the western side of the circle), gradients might still be present. Thus, from the differences in the NO₂ VCDs derived from the car MAX-DOAS measurements themselves, only a lower limit of the errors caused by a gap can be estimated.

One simple way to estimate such errors is to perform the summation (Eq. 2) in two directions and compare the corresponding results as in Shaiganfar et al. (2011). Since the values of the wind speed and direction in Eq. (2) are determined for the location of measurement i , but the distance Δs_i is determined between measurement i and $i + 1$, the direction for which the sum is calculated leads to a difference in the derived total NO₂ flux. For this reason, we use the average NO_x emissions from both directions for the determination of the NO_x fluxes in our study. If no gaps are present (or if the NO₂ VCDs on both sides of a gap are similar), the results for both directions are almost the same. But for large gaps and large differences in the NO₂ VCDs on both sides of the gap, the differences become large. For the measurements shown in Fig. 4a the difference in the results for both directions is 25 %. Note that for most measurements the differences are much smaller. In Sect. 4.6.1, we develop a more sophisticated method for the determination of the errors caused by gaps.

In Fig. 4b an example of measurements without an obvious gap is shown. However, on that day a large difference between the NO₂ VCD between the start and end locations of the circle is found, indicating that during the period of the measurements the NO_x distribution around the location of the maximum outflux has changed significantly. Obviously, the NO_x emissions derived from these measurements are subject to large uncertainties and are thus also left out of the set of measurements considered for the comparison with the input emissions (Sect. 6).

4.3 Partitioning correction

Since NO cannot be measured by car MAX-DOAS measurements, but we are interested in the total NO_x (NO + NO₂) emissions, the NO₂ fluxes derived from Eq. (2) have to be multiplied by a partitioning correction factor:

$$F_{\text{NO}_x} = F_{\text{NO}_2} \cdot c_p, \quad (4)$$

with

$$c_p = \frac{[\text{NO}_2] + [\text{NO}]}{[\text{NO}_2]}. \quad (5)$$

The partitioning correction factor is typically between 1.1 and 2 and can be derived from, e.g., model simulations (e.g. from the ratio of the respective VCDs) like in this study. If no model data are available, standard values for typical situations (e.g. Seinfeld and Pandis, 2012) can be used. The partitioning of NO and NO₂ depends mainly on the ozone concentration and the solar radiation. For a high ozone concentration and low actinic flux, a higher fraction of NO_x is in the form of NO₂ (and vice versa). Figure 5 presents NO₂ VCDs derived from the car MAX-DOAS measurements (panel a) and partitioning ratios derived from simultaneous model simulations for 8 February 2010. Interestingly, the highest partitioning ratios are found at the same locations as the maximum NO₂ VCDs. In the following, we always use the partitioning ratios from the model simulations at the locations of the maximum NO₂ VCDs for the conversion of the NO₂ fluxes into NO_x emissions (Eq. 4) because the derived NO_x emission fluxes depend mainly on the difference between the maximum NO₂ VCDs (on the downwind side) and the background values.

Figure A3 presents the partitioning ratios derived from the model simulations (ratio of the respective VCDs) at the locations of the maximum NO₂ VCDs for all days of both seasons. In summer, on average, smaller partitioning ratios (1.32) than in winter (1.51) are found, probably related to the higher ozone mixing ratios in summer (see Fig. A4). The results in Fig. A3 indicate a general problem: the deviations of the daily values from the seasonal average values are up to 30 %, and this rather large uncertainty directly propagates to the derived NO_x emissions via Eq. (4).

One possibility to constrain the daily partitioning ratios might be to use the dependency on the wind speed (see Fig. 6). Here, it should be noted that the partitioning ratios in Fig. 6 are normalised (divided) by the seasonal averages in order to make the values for both seasons directly comparable. Decreasing (normalised) partitioning ratios (i.e. increasing relative contributions of NO₂ to the total NO_x) are found with increasing wind speed and vice versa. This finding is probably caused by a more effective turbulent mixing for days with higher wind speeds, which allows a more effective transport of ozone-rich air into the air parcels with high NO concentrations. Indeed higher ozone concentrations and tropospheric column densities are found for higher wind speeds (see Figs. A4 and A5).

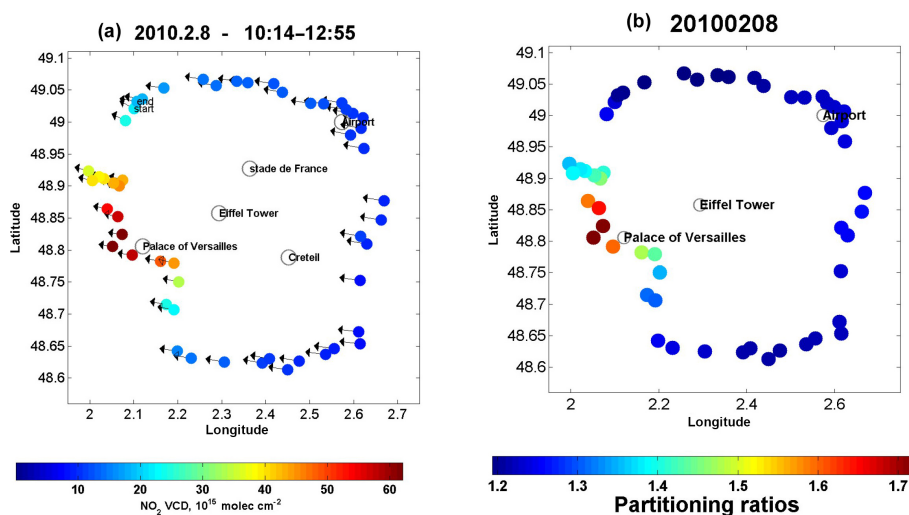


Figure 5. (a) NO₂ VCDs retrieved from car MAX-DOAS measurements on 8 February 2010. (b) Partitioning ratios (NO_x / NO₂) derived from model simulations at the locations of the car MAX-DOAS observations. High partitioning ratios are found at the same locations of the maximum NO₂ VCDs.

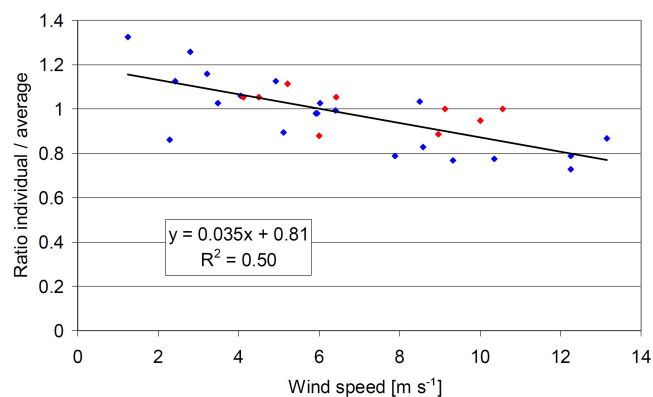


Figure 6. Dependence of the normalised partitioning ratios on wind speed (the individual ratios are divided by the seasonal average). Red points represent summer and blue points winter data.

4.4 Effect of NO_x lifetime

Because of the generally short lifetime of NO_x in the boundary layer, part of the emitted NO_x is destroyed during the transport of the air masses from the emission source to the location of the measurement. Thus, the emissions derived from the measured NO₂ VCDs underestimate the true emissions. To correct for this underestimation, Shaiganfar et al. (2011) applied a so-called lifetime correction factor:

$$c_{\tau} = e^{\frac{r}{v \cdot \tau}}. \quad (6)$$

It is calculated from the wind speed v , the distance r between the city centre and the location of the highest NO₂ VCDs, and the lifetime τ . For the measurements around Paris, we assume a NO_x lifetime of 3 and 12 h in summer and winter,

respectively (see, e.g., Beirle et al., 2011). Here, it should be noted that these lifetimes are rough assumptions, and on individual days large deviations from the assumed values might occur. Moreover, in a strict sense separate lifetime corrections should be applied for individual height layers. But especially for wind speeds above about 2 m s⁻¹, the effect of the limited lifetime of NO_x and thus of the uncertainties in the assumed lifetimes, are small (the correction factor is close to unity). Only in cases with low wind speeds do larger effects occur (see Fig. 7). Here, it is interesting to note that for our measurements the effect of the wind speed dominates the variability in the lifetime correction factor, while the distance between the emission source and the measurements has only a small influence (Fig. A6). The errors in the derived NO_x emissions caused by the uncertainties in the lifetime are discussed in more detail in Sect. 4.6.4.

4.4.1 Lifetime correction for the influx

Shaiganfar et al. (2011) applied the lifetime correction only for the total emissions from the encircled area (difference between influx and outflux). However, in cases with a high influx of NO_x, a lifetime correction should also be applied for the influx of NO_x because only part of the NO_x which is transported into the encircled area will actually reach the location of the outflux measurement. In such cases (see example in Fig. 8), the total flux will be underestimated if no lifetime correction for the influx is performed. In most cases, however, the influx of NO_x is rather small, and thus neglecting the lifetime correction for the influx only has a small effect (a few percent) on the derived emissions.

We tested two versions of the lifetime correction for the influx. In the basic version, a lifetime correction factor was

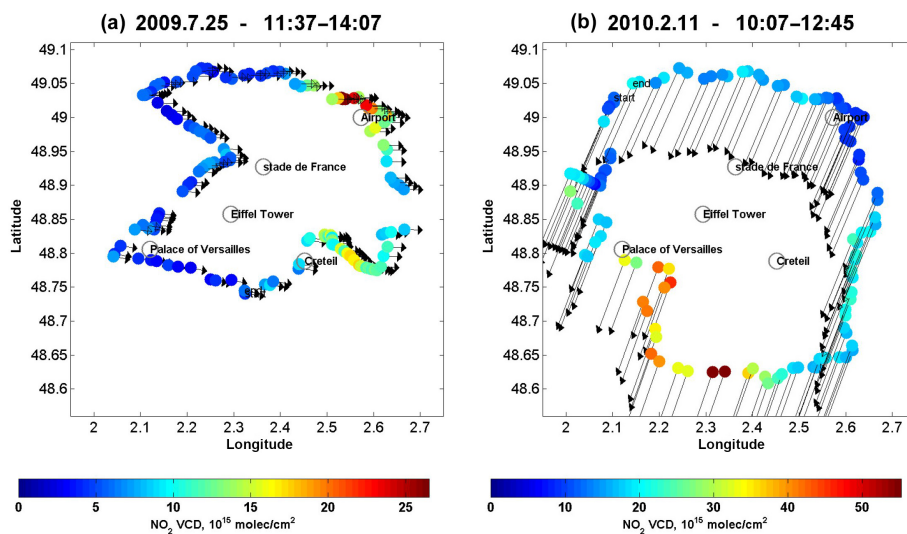


Figure 7. Measured NO₂ VCDs and corresponding wind vectors for 2 selected days with extreme lifetime correction factors. Dates are given as yyyy.m.dd. For the day with low wind speed (a), a high lifetime correction factor of 1.71 is found, and for the day with high wind speed (b), a low lifetime correction factor of 1.05 is found.

determined in the same way as for the outflux and the inverse of the lifetime correction factor was applied to the derived NO_x influx before it was subtracted from the outflux. In the more sophisticated version, the lifetime correction was only applied to the enhancement of the NO₂ VCDs over the minimum NO₂ VCDs on the upwind side. This procedure takes into account that a large part of the observed NO₂ VCDs actually represents a homogenous background concentration, which is present on both the upwind and downwind sides. This NO_x background is probably mostly located in the free troposphere, where the atmospheric lifetime is longer than in the boundary layer. Thus, the lifetime correction was only applied to the enhancements over this background.

To demonstrate the effect of the lifetime correction for the influx, we calculated the NO_x emissions for 28 January 2010 (Fig. 8) in three ways:

- without a lifetime correction for the influx – the resulting NO_x emissions are 8.53×10^{25} molec s⁻¹.
- with the basic lifetime correction for the influx – the resulting NO_x emissions are 9.68×10^{25} molec s⁻¹.
- with the sophisticated lifetime correction for the enhancements over the background – the resulting NO_x emissions are 9.05×10^{25} molec s⁻¹.

In the following, we apply the sophisticated version of the lifetime correction of the influx for all days. Here, it should however be noted that the example shown in Fig. 8 is a rather extreme case, and for most of the days the effect of the influx correction is small (a few percent). However, it should also be noted that a lifetime correction for the influx is especially important for measurements with small differences between the outflux and influx.

4.5 Emission upscaling using nighttime lights

Like in Shaiganfar et al. (2011), the spatial distribution of nighttime lights (NOAA, National geophysical Data Center, <https://ngdc.noaa.gov/eog/>; Ziskin et al., 2010) measured by satellite was used to upscale the derived NO_x emissions to a defined area around the city of interest. The corresponding distribution around Paris is shown in Fig. 9. The upscaling factor is defined as

$$C_{\text{upscaling}} = \frac{L_{\text{full area}}}{L_{\text{circle}}}. \quad (7)$$

Here, $L_{\text{full area}}$ is the integral of the nighttime lights over the full area (latitude–longitude ranges as shown in Fig. 9) and L_{circle} is the integral over the area inside the circle used for the car MAX-DOAS measurements. For most days during the MEGAPOLI campaign, the driving routes included large parts of the city, and the corresponding upscaling factors are between 1.23 and 2.11.

In addition to the upscaling factors calculated using the nighttime lights, we also calculated upscaling factors based on the distribution of NO_x emissions in the emission inventory used for the model simulations (see Fig. 2). A scatter plot of both upscaling factors is shown in Fig. 10. The slope of the regression line and the correlation coefficient (r^2) are close to unity, but the scatter increases slightly with increasing upscaling factors. This finding is not unexpected, taking into account the different quantities used for the upscaling (and also their different spatial resolutions). Especially for small circles, large deviations between the spatial distributions of nighttime lights and the NO_x emissions are expected, e.g. due to the effect of strong and localised emission sources (e.g. power plants), which are not well represented by the

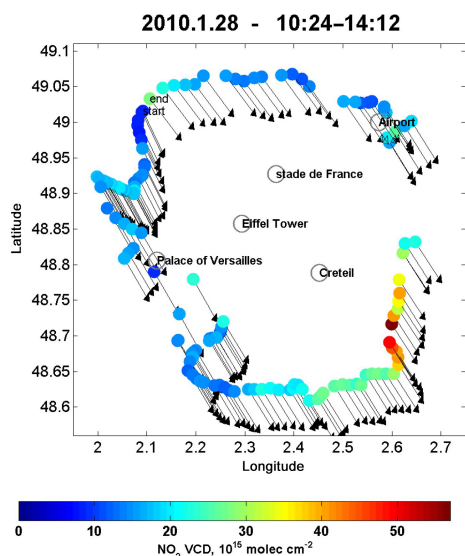


Figure 8. NO₂ VCDs measured on 28 January 2010. On this day locally enhanced NO₂ VCDs are found on the upwind side of the circle.

nighttime lights. The location and type of the strongest point sources is presented in Table 1.

4.6 Error estimation

In the previous subsections several steps for the calculation of NO_x emissions from car MAX-DOAS observations were discussed. Each of these steps is subject to specific uncertainties. Some of these uncertainties are directly related to each other, e.g. the uncertainties in the wind speed and the lifetime correction. The following main uncertainties for the determination of the NO_x emissions can be identified.

a. Sampling effects:

- measurement gaps
- small circles causing large upscaling factors
- time difference between measurements of influx and outflux.

b. Measurement uncertainties:

- errors in the derived NO₂ VCDs.

c. Meteorological effects:

- errors in residence time over the area, especially for low wind speeds
- changing wind speeds and wind directions.

d. Chemical effects:

- uncertainties in the lifetime correction factor
- uncertainties in the partitioning ratio.

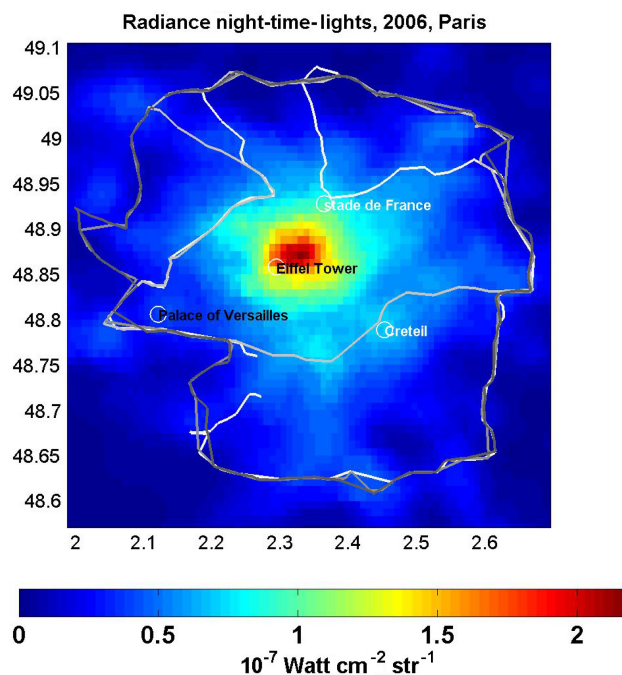


Figure 9. Spatial distribution of the nighttime lights for the selected area around Paris. Different driving routes for 2 days in summer and 2 days in winter are shown.

Some of these error sources can be minimised by an optimised planning of the driving routes. In particular, measurements should be performed around rather large circles, and bows close to the city centre should be avoided. Other factors like the meteorology cannot be influenced by the experimentalists. But based on the meteorological conditions, decisions about when measurements are meaningful or not could be made (especially situations with very low wind speeds or highly varying wind fields should be avoided). While the lifetime correction factors can usually be calculated with low uncertainties (except for very low wind speeds), the uncertainties caused by the partitioning factor can be large. The effect of the time difference between the measurements of the influx and outflux can in general be neglected because the temporal variability in the background is rather low. It must, however, be taken into account that the derived NO_x emissions are only representative of a specific time period of the day (mainly depending on wind speed and the diameter of the driving circle; see also Sect. 5). In the following, the different error sources are quantified in more detail.

4.6.1 Errors caused by gaps in measurements

Due to the finite number of measurements, the total flux of NO₂ has to be determined by a sum (Eq. 2) instead of an integral (Eq. 1); i.e. at a given location i , the derived VCD _{i} is applied along the complete distance Δs_i towards the next lo-

cation. In case of large distances Δs_i (“gaps”), this procedure introduces uncertainty in the resulting emissions.

As shown in Sect. 4.2 problems caused by large gaps can be identified in a simple way by comparing the emissions calculated in opposite directions along the driving route (Eq. 2). In the following, we present a more sophisticated way of quantifying the uncertainties related to gaps, based on error propagation.

In order to estimate the error in F due to gaps, we use the following approach.

First we estimate the uncertainty in VCD simply by the standard deviation (SD) of all measurements VCD_i ,

$$\Delta VCD = SD(VCD_i), \quad (8)$$

and thus the error in a single summand in Eq. (2) as

$$\Delta VCD_i \cdot \omega_i \cdot \sin(\beta_i) \cdot \Delta s_i. \quad (9)$$

The error in the flux is then given as

$$\begin{aligned} \Delta F &= \sqrt{\sum_i (\Delta VCD_i \cdot \omega_i \cdot \sin(\beta_i) \cdot \Delta s_i)^2} \\ &= \Delta VCD \cdot \sqrt{\sum_i (\omega_i \cdot \sin(\beta_i) \cdot \Delta s_i)^2}. \end{aligned} \quad (10)$$

This approach assumes that the error in the single summands can be estimated from the statistical distribution of VCDs, assuming them to be independent. In reality, however,

1. VCDs for neighbouring locations are generally correlated, and
2. the variability in VCDs (and thus the potential error caused by gaps) is generally higher for the outflow than for the inflow.

To account for this, we modify the error estimate by

1. ignoring summands with $\Delta s_i < 3$ km in Eq. (10) (terms with sufficient spatial sampling should not contribute) and
2. calculating the uncertainty in in- and outflow separately (defined only by the sign of the individual summands). For the inflow, ΔVCD , and thus ΔF , is generally lower than for the outflow.

The total uncertainty is then given only by the root of the sum of squares of the uncertainties in in- and outflow. This results in a realistic error estimate for errors introduced by gaps, as long as the SD reflects the true uncertainty; i.e. the existing measurements actually reflect the variability in the NO₂ distribution.

4.6.2 Errors caused due to upscaling

As shown in Sect. 4.5 the error in the upscaling factor increases with increasing upscaling factor (for small circles). We suggest describing the error in the upscaling factor by the following empirical formula:

$$\text{error}_{\text{upscaling}} = (c_{\text{upscaling}} - 1) \cdot 0.4. \quad (11)$$

By this simple formula it is ensured that for a (hypothetic) driving route encircling the whole area (upscaling factor = 1) the uncertainty in the upscaling factor would be 0 and that for increasing upscaling factors, the uncertainties also increase (up to about 45 % for the largest upscaling factor used in this study). In Fig. 10 it was shown that the deviation of the upscaling factors derived from the spatial distribution of the nighttime lights or the emission inventory differs by about 10 % for large upscaling factors. Thus, our formula probably overestimates the uncertainties caused by the application of the scaling factor. Note that for other locations with different spatial patterns of the NO_x emissions, this simple parameterisation might not be appropriate.

4.6.3 Errors caused by the variability in the wind field

We quantify errors related to variations in the wind field by calculating the NO_x emissions not only for the average values of the wind speed and wind direction (see Sect. 4.1) but also for wind speeds changed by ± 2 m s⁻¹ and wind directions changed by $\pm 20^\circ$. Such variations are often found for measurements around full circles for the Paris measurements. Here, it should be noted that the assumed variations in wind speed and direction are also partly accounted for by uncertainties in the assumed NO_x height profiles (see Sect. 4.1), since wind speed and direction change with altitude.

In Fig. 11, 2 days with extremely variable wind fields are shown. On 24 January 2010 (panel a) the wind speed changed by more than a factor of 2; on 29 January 2010 (panel b) the wind direction changed by more than 60° during the driving route along the circle. For both days, large differences in the NO_x emissions derived using either averaged or variable wind data were obtained (36 % for 24 January; more than 100 % for 29 January).

We also determined the NO_x emissions using the spatio-temporally varying wind fields (interpolated to the exact locations and times of the individual car MAX-DOAS measurements) and compared them to the results derived from using the averaged wind data. Figure 12 displays the relative differences in the derived NO_x emissions with either averaged or spatio-temporally varying wind fields for all days versus the wind-related errors, calculated as described at the beginning of this subsection. For most days, the relative differences are small (< 10 %), but larger differences are found for days with large errors caused by the variability in the wind fields (see also Fig. A7). This is an important finding because it indicates that the errors caused by the variability

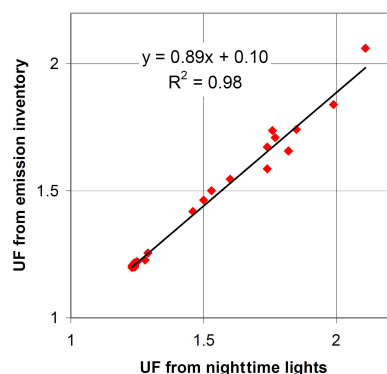


Figure 10. Upscaling factors (UF) based on the distribution of the NO_x emissions are plotted as a function of the upscaling factor based on nighttime lights.

in the wind field are well represented by the simple approach to estimate the wind-related errors. Also, for days with small wind-related errors the averaged wind speed and direction can be used well without introducing significant additional errors. Here, it should be noted that spatio-temporally resolved wind data are usually not available.

4.6.4 Errors caused by the lifetime correction

Similar to the errors caused by variations in the wind field, the errors caused by uncertainties in the lifetime correction were also calculated. Here, we assumed variations in the lifetime of $\pm 25\%$. It should be noted that this deviation should be seen as a rough estimate of the uncertainty in the lifetime, and on individual days the deviations from the assumed values might be larger. However, as shown in Sect. 4.6.6, the errors caused by uncertainties in the lifetime are generally much smaller than those from other error sources. Thus, our choice of the lifetime uncertainty is not critical.

4.6.5 Errors caused by the partitioning correction

In this study we derived the partitioning ratios from the model data. We found that the partitioning ratios depend systematically on season but also vary from day to day (Fig. A3). The day-to-day variation probably mainly reflects variations in meteorology and solar radiation, which affect the local partitioning ratios. For summer, an average partitioning ratio of 1.32 and for winter of 1.51 is found. These values might serve as first-guess values also for other campaigns. A further refinement could be derived from the dependence of the partitioning ratio on wind speed (Fig. 6). But the validity of this dependence should be investigated in more detail in future studies.

Furthermore, it should be noted that close to strong emission sources (like power plants), only a limited fraction of the NO might be already converted to NO₂ due to the titration of O₃. In such cases, the total NO_x emissions will be

systematically underestimated by our method. As discussed in Shaiganfar et al. (2011), the efficiency of the mixing of ozone-rich air with the NO_x emission plume depends on the atmospheric stability and wind speed. As a rule of thumb, the distance of the car MAX-DOAS measurements from strong emission sources should be about ≥ 5 km (see also Shaiganfar et al., 2011). In this study we used individual partitioning ratios derived from the model results (see Sect. 4.3). The respective uncertainties are difficult to quantify, and in the following, we assume a value of 15 %, which reflects the scatter of the daily values around the fitted regression line in Fig. 6. If no model simulations are available, the corresponding uncertainties might be substantially larger, but part of the variability might be parameterised by the wind speed.

4.6.6 Total error

In Fig. 13 the errors discussed in this section are shown for all days of the MEGAPOLI campaigns. On most days the errors caused by the variability in the wind field and due to gaps dominate the total uncertainties. Total errors range from ± 30 to $\pm 50\%$.

5 Consistency check based on CHIMERE model simulations

Based on the CHIMERE model simulations the consistency of CIM can be checked. For that purpose first the NO₂ VCDs for the exact locations and times of the car MAX-DOAS measurements were extracted. Then the CIM was applied to the extracted model NO₂ VCDs in the same way as for the measurements. The derived NO_x emissions were compared to the TNO-MEGAPOLI emissions used as input for the model simulations (Fig. 2). Here, the input emissions for the individual time periods of the measurements were selected: the time of the observations of the maximum NO₂ VCDs was used as the end of the time periods. The beginning of the time period was determined relative to the end time by subtracting the transport time of the air masses from the city centre to the location of the maximum NO₂ VCDs. By selecting this time period, we take into account the average travel time of the polluted air masses until the location of the measurement. The corresponding time periods range from 2 to 4 h. Here, it is interesting to note that for the cases considered, time variations of ± 1 h lead to changes in the respective input emissions of 2 to 15 %.

The results for the consistency check are shown in Fig. 14. There, the ratios of the derived emissions (CIM) versus the emissions (TNO) are displayed. Most of the ratios are close to unity, especially if their error bars (see Sect. 4.6) are considered. However, for several days large deviations (over- or underestimation) are also found. For most of these days, the errors are also larger than on the other days.

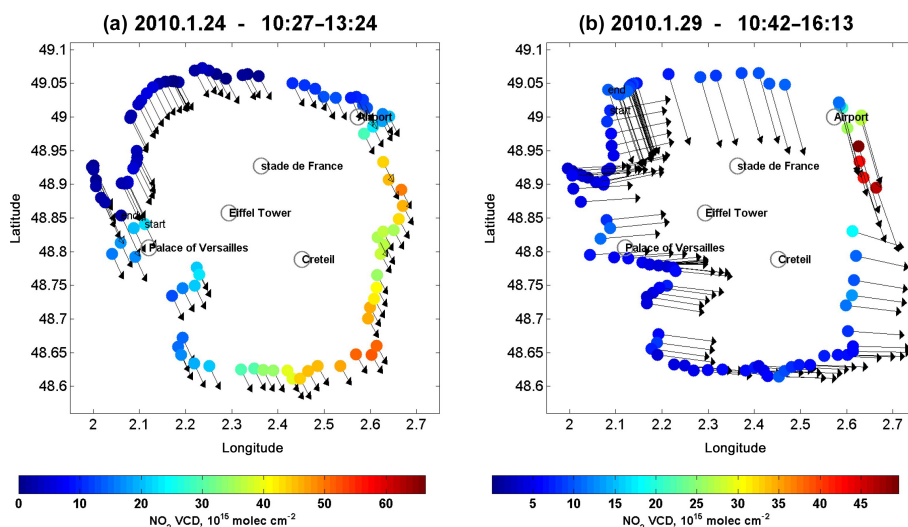


Figure 11. Measured NO₂ VCDs and corresponding wind vectors for 2 selected days with extremely variable wind fields. On 24 January 2010 (a) the wind speed and on 29 January 2010 (b) the wind direction showed large variations.

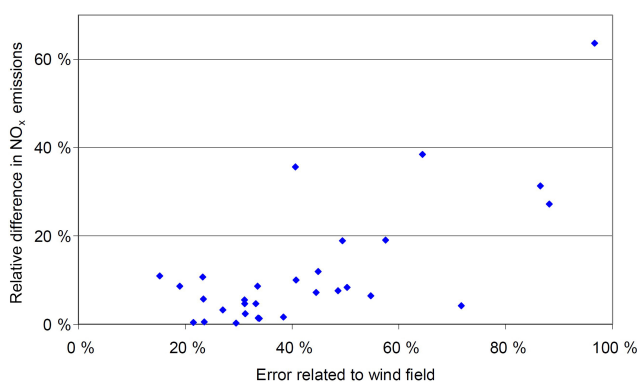


Figure 12. Difference in the NO_x emissions derived from either averaged or variable wind data plotted versus the wind-related error calculated as described in Sect. 4.6.3.

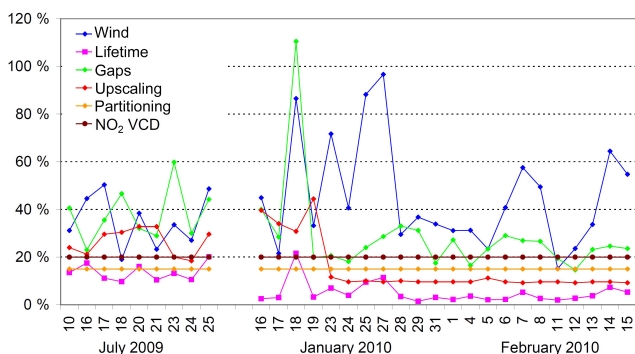


Figure 13. Individual errors derived for all car MAX-DOAS measurements considered in this study.

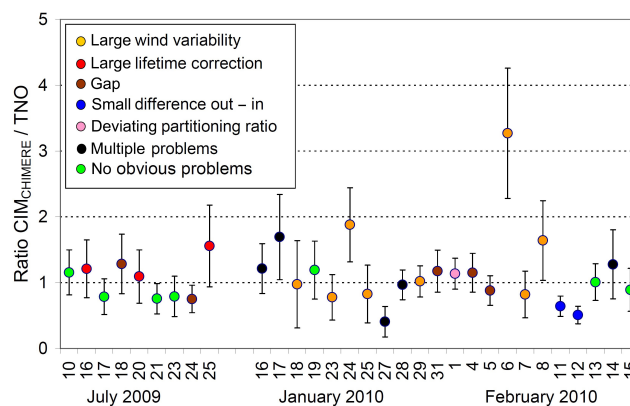


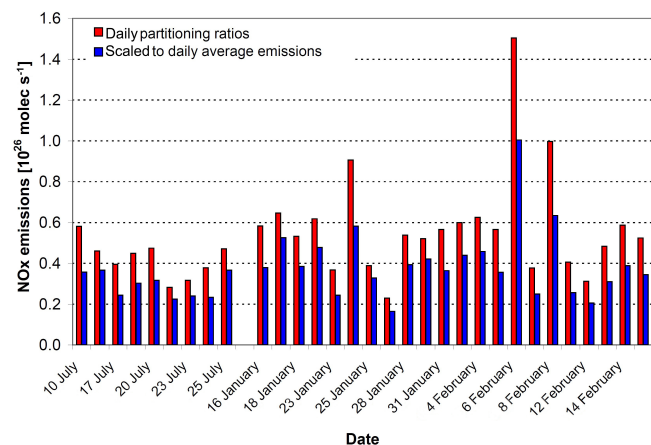
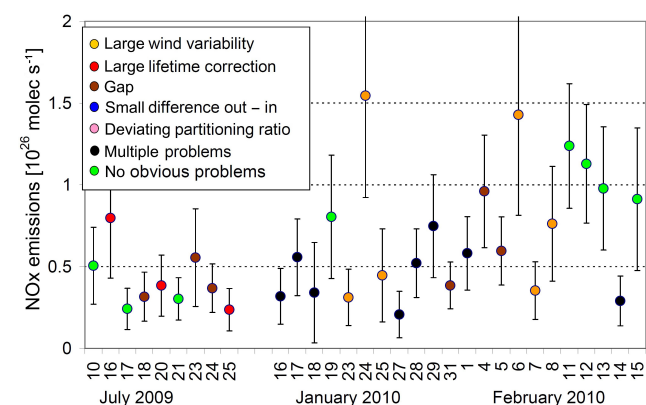
Figure 14. Ratios of the derived NO_x emissions (CIM_{CHIMERE}) and the TNO emissions used for the model simulations. For the CIM individual partitioning ratios for the different days are used (see Sect. 4.3). The TNO emissions are averaged for the time period of the respective measurements (see text). The colours indicate different kinds of problems of the individual days (see also Table 3).

It is interesting to relate the derived ratios to the contribution of specific problems affecting the CIM (see Sect. 4.6). For that purpose, in Fig. 14 different problems are indicated by different colours (for the criteria used for the identification of the different problems, see Table 2).

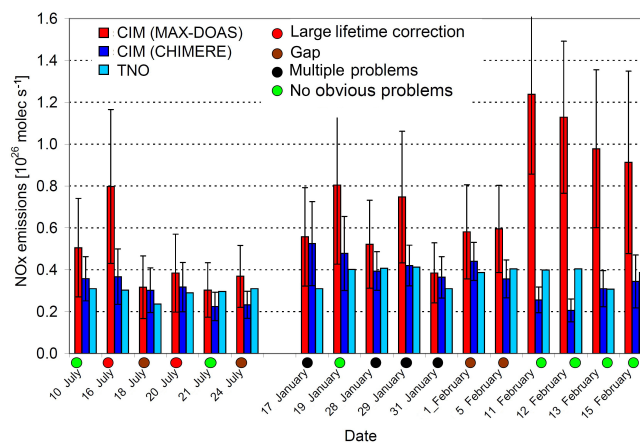
For days with no obvious problems (green dots), the ratios are in general close to unity and the error bars are rather small. The largest deviations from unity are found for days with large variability in the wind field. For days with small differences between the outflux and the influx, ratios below unity were typically derived, and for days with large lifetime corrections, ratios larger than unity were typically obtained. For the other problems, no clear systematic effects

Table 2. Criteria used for the identification of different problems.

Problem	Criterion
Large wind variability	Relative deviation of wind speed ($v_{\max} - v_{\min}$) > 30 %; deviation of wind direction > 30°
Large lifetime correction	Lifetime correction factor > 1.5
Gap/route close to the centre	Gaps > 14 km or ratio of NO ₂ flux left/right between 0.80 and 1.20
Small difference between influx and outflux	Ratio outflux / influx (NO ₂) < 1.3
Large partitioning ratio	Relative difference to seasonal average value larger than ± 25 %

**Figure 15.** Comparison of the derived emissions from CHIMERE model simulations for either the periods of the individual measurements or scaled to daily averages. Days with uncertainties in the car MAX-DOAS measurements > 100 % and with ratios of the CIM results for CHIMERE and TNO emissions above 1.7 and below 0.6 are left out.**Figure 16.** NO_x Emissions derived from the car MAX-DOAS measurements (using individual partitioning ratios and scaled to daily average values). The colours of the data points indicate different error sources (see also Table 3).

were found. Here, it should be noted that the choice of the selection criteria for the different problems is somewhat arbitrary, but the selection criteria described in Table 3 might

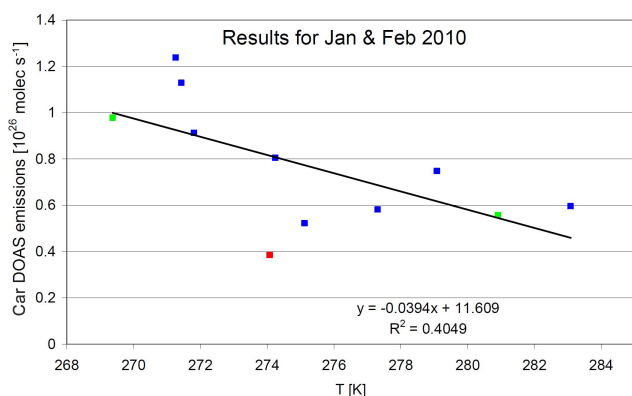
**Figure 17.** Comparison of the NO_x emissions derived from the car MAX-DOAS measurements (red) with the CHIMERE model simulations (blue) and the corresponding TNO input emissions (light blue). All data represent daily average emissions. The NO_x emissions from MAX-DOAS and CHIMERE were derived using daily partitioning ratios. Results are only shown for “good” measurement days (days with uncertainties in the car MAX-DOAS measurements > 100 % and with ratios of the CIM results for CHIMERE and TNO emissions above 1.7 and below 0.6 are left out). The coloured disks below the bars indicate potential problems of specific days (same scheme as in Fig. 16). Note that the following days are weekend days: Saturdays – 18 July, 17 January, 13 February; Sundays – 31 January.

serve as a first orientation on whether a given measurement is suitable or not for the application of the CIM.

We further investigated possible reasons for the deviation of the ratios of the CIM results and the TNO-MEGAPOLI emissions from unity. For that purpose we display the ratios as a function of the different quantities, which might affect the determination of the NO_x emissions (Fig. A8). For most of these quantities no or only a weak correlation is found (especially for the winter data). For the summer data, higher correlations, especially versus the lifetime correction factor and the partitioning ratio, are found, indicating a possible over- or under-correction of the respective influences. However, because the correlations are still rather weak and are based only on few data points, we did not make any change to our assumptions made for the lifetime correction (Sect. 4.4).

Table 3. Overview of days with several problems.

Day	Model simulations	MAX-DOAS measurements
18/07/2009		Large gap; large difference left/right
16/01/2010	Large difference left/right; deviating partitioning ratio	Large difference left/right; deviating partitioning ratio
17/01/2010	Large gap; deviating partitioning ratio	Large gap; deviating partitioning ratio
27/01/2010	Large wind variability; large difference left/right; small difference out-in	Large wind variability; large difference left/right; small difference out-in
28/01/2010	Large gap Small difference out-in; deviating partitioning ratio	Large gap; deviating partitioning ratio
29/01/2010	Deviating partitioning ratio; large wind variability	Large difference left/right; deviating partitioning ratio; large wind variability
01/02/2010		Large difference left/right; deviating partitioning ratio
14/02/2010	Large difference left/right; large wind variability	Large difference left/right; large wind variability

**Figure 18.** NO_x emissions derived from car MAX-DOAS observations in winter as a function of the surface temperature (average temperature taken from the model simulations during the period of the car MAX-DOAS measurements). Green and red dots mark results for Saturdays and Sundays, respectively.

Finally, we converted the emissions derived for different time periods of the day to the daily average values according to the respective diurnal variations in the emission input data (Fig. 2). The resulting daily average NO_x emissions together with the NO_x emissions derived for the periods of the measurements are shown in Fig. 15. The daily average values are in general smaller than the emissions during the period of the measurements because the measurements are always made during the day, while the minimum of the emissions is found during night (Fig. 2). The ratio of the average summer values to the average winter values (0.58) is systematically lower than the same ratio in the emission inventory for Paris (0.81; see also Fig. 2a). Interestingly, on most weekend days (Saturdays: 18 July, 17 January, 13 February; Sundays: 31 January) the lowest emissions were not found, indicating that the variation in the NO_x emissions derived from car MAX-DOAS is not dominated by the weekend effect. (Fig. 17)

6 Application to measurement data

In Fig. 16, the NO_x emissions and the associated errors derived from the car MAX-DOAS measurements for all days during both campaigns are shown. In contrast to the results from the model simulations (Fig. 14), the errors also include the uncertainties in the determination of the NO₂ VCD (20%). Thus, the error bars are in general larger than those in Fig. 14. Potential problems for individual days are indicated by the colours of the data points.

Like for the results derived from the model simulations, for the car MAX-DOAS the smallest errors are also in general found for days without obvious problems. However, the variability in the derived NO_x emissions is larger than for the results derived from the model simulations, indicating that the real variability in the emissions is probably larger than that of the model results. However, it should also be noted that most of the results could be reconciled taking the error bars into account.

In Fig. 17 the daily average emissions derived from car MAX-DOAS measurements are compared to those derived from the model simulations and to the TNO emissions. Note that only results for days with small uncertainties and small differences between CIM results for CHIMERE and TNO emissions are shown (14 days of 31 days with uncertainties in the car MAX-DOAS measurements > 100% and with ratios of the CIM results for CHIMERE and TNO emissions above 1.7 and below 0.6 are left out). In general, higher NO_x emissions are derived from the car MAX-DOAS measurements than from the CHIMERE model simulations (and also compared to the TNO emissions). The differences between the car MAX-DOAS and CHIMERE results are higher in winter (about a factor of 2.1) than in summer (about a factor of 1.5). Here, it is interesting to note that the highest emission estimates from car MAX-DOAS observations in winter are found for 4 cold days in mid-February (see Figs. 17 and 18). On most of these days, strong northerly winds also occurred (see Fig. A9). If only the other days in winter are con-

Table 4. Comparison of the daily average NO_x emissions from TNO with those derived from CHIMERE (CIM_{CHIMERE}) and car MAX-DOAS (CIM_{MAXDOAS}) for days with errors in the car MAX-DOAS data < 100 % and differences in the CIM results for CHIMERE and TNO emissions < 70 %. For the calculation of the average, the daily values are weighted by their individual errors. The values in brackets are calculated for all days. Emissions are given as 10²⁵ molec NO_x per second.

Season	TNO	CIM _{CHIMERE}	CIM _{MAXDOAS}	Ratio CIM _{MAXDOAS} / CIM _{CHIMERE}
Summer	2.9 (2.9)	2.9 (2.8)	4.0 (3.6)	1.38 (1.29)
Winter	3.8 (3.6)	3.4 (3.6)	6.9 (5.7)	2.03 (1.58)

sidered, a similar ratio (1.4) of the NO_x emissions from car MAX-DOAS to those derived from the CHIMERE model as in summer is derived. The effect of temperature on the NO_x emissions will be discussed in more detail in the next section.

7 Conclusions and perspectives

We applied the CIM for the determination of the NO_x emissions from Paris based on a large set of car MAX-DOAS measurements during two measurement campaigns in summer 2009 and winter 2009/2010. The campaigns were organised within the framework of the European project MEGAPOLI (Baklanov et al., 2011; see also <http://megapoli.dmi.dk/>). The CIM was applied to car MAX-DOAS measurements made in large circles around Paris with diameters of about 20 to 40 km. On 9 days in summer 2009 and 22 days in winter 2009/2010, meaningful emission estimates were possible. Compared to previous applications of the CIM, the large number of measurements (together with the model results) during the MEGAPOLI campaign allowed us to investigate important aspects of the CIM. In particular, the applicability of the CIM under various atmospheric conditions could be tested. Another important advantage of the MEGAPOLI campaigns is that simultaneous atmospheric model simulations of the CHIMERE model with a high spatial resolution (3 × 3 km²) were available for all days. Based on these model data it was, in particular, possible to test the consistency of the CIM. For that purpose the model data were first sampled at exactly the same locations and times as the car MAX-DOAS measurements. Then the CIM was applied to the extracted model results and the corresponding NO_x emissions are determined. Finally the derived emissions were compared to the input emissions used in the model simulations. From this consistency check important information about favourable or non-favourable conditions for the application of the CIM was derived. In most cases, the errors caused by uncertainties and the variability in the wind fields contribute most to the total error budget. From this finding we conclude that particular situations with low wind speeds and/or large variability in the wind directions should be avoided. Also, gaps and uncertainties in the partitioning ratio are important error sources. Based on the consistency check, we also deduced a set of criteria on whether measure-

ment conditions are suitable or not for the application of the CIM. We also discuss the individual steps of the CIM, in particular the effect of lifetime correction (for the influx and outflux) and the correction for the partitioning of NO and NO₂, and developed methods to calculate the error budget of the derived NO_x emissions. From the consistency check based on the CHIMERE model, we found that the derived total errors are consistent with the deviations between the emissions derived from the application of the CIM to the model data and the input emissions (TNO-MEGAPOLI). Typical errors are between ±30 and ±50 %.

We applied the CIM to car MAX-DOAS observations for summer and winter. In summer, daily average NO_x emissions of 4.0 × 10²⁵ molec s⁻¹ and, in winter, daily average NO_x emissions of 6.9 × 10²⁵ molec s⁻¹ were derived for Paris. These values are a factor of about 1.4 and 2.0 larger than the corresponding input emissions (and also the emissions derived from the application of the CIM to the model data) in summer and winter, respectively (for several days these deviations are larger than the error bars). Similar ratios are also found for the comparison with the TNO Monitoring Atmospheric composition and climate III (MACC-III) inventory (1.5 and 2.3 for summer and winter, respectively). These findings contradict previous comparison studies based on ground-based (Zhang et al., 2013) and aircraft measurements (Petetin et al., 2015), which found that the model simulations systematically overestimate the measurements for July 2009. The reason for the systematic discrepancies with our results is not clear. One probable reason is that our measurements are sensitive to the integrated NO₂ concentration in about the lowest 3 km of the atmosphere, while the previous studies compared in situ observations at the ground or between about 500 and 900 m altitude. Here, it is interesting to note that similar ratios between the emissions derived from the car MAX-DOAS data and CHIMERE results were also found for the direct comparison of the NO₂ VCDs derived from car MAX-DOAS or CHIMERE (Shaiganfar et al., 2015), indicating that the differences between the measurements and the model simulations are not caused by the application of the CIM. Other interesting findings are the enhanced seasonal cycle and the larger day-to-day variability in the NO_x emissions derived from the car MAX-DOAS measurements compared to those of the input emissions (see

Fig. 2). Here, it is interesting to note that a high day-to-day variability was also found by Petetin et al. (2015). For most of the measurement-derived emission results, the day-to-day variability is within the range of the uncertainties, especially in summer. Thus, we conclude that this variability simply reflects the uncertainty range of the measurements. However, for several days at the end of the winter measurement campaign in mid-February, significantly enhanced values were found compared to the other winter days. These days are also the reason for the rather high average values derived from the car MAX-DOAS measurements in winter. If these days are excluded, a similar ratio (1.4) of the NO_x emissions derived from car MAX-DOAS or CHIMERE as in summer (1.5) is found. Interestingly, for these days the temperature was low (−4 to −1 °C), indicating that the high emissions might be related to these low temperatures (see Fig. 18). The following effects might be responsible for enhanced NO_x emissions on cold days.

a. Residential heating

According to Fig. 2 domestic heating contributes about 25 % to the total NO_x emissions in winter. If one assumes a factor of 2 variability between cold and warm (less cold) winter days (see, e.g., Terrenoire et al., 2015), it becomes clear that the variability in the NO_x emissions from residential combustion alone can only explain a part of the increase of about a factor of 2 found for the cold days.

b. Temperature dependence of catalytic converters

During winter time, NO_x emissions from traffic contribute about half to the total NO_x emissions. Under cold conditions, three-way catalytic converters for gasoline cars work less well, and they take a longer time to reach to an optimised way of working for diesel cars (the cold-start effect). It is probable that this effect leads to increased NO_x emissions on cold days, but this additional emission is difficult to quantify.

c. It is known that in the past during cold periods an older 250 MW coal-fired power plant was temporarily restarted to meet the additional demand for electrical heating in the city. Several other fuel- or gas-driven combustion turbines can also be activated during periods of increased energy demand. On an annual basis, such temporarily operating facilities would not add much to the annual total emissions, but during certain episodes, they could be important. Instead of being spread out over the year, the emissions would have to be allocated to a much smaller number of operation days, causing the emissions during selected periods to be much higher than the annual average and in other moments to be zero. Unfortunately, we have no access to operation days for such facilities and cannot confirm that this contributed also during the February episode discussed in this paper.

While we have explored the uncertainties associated with the car MAX-DOAS measurements in this paper, it should be acknowledged that exact emission timing per hour or per day in the emission inventories is also rather poorly defined. The time profile (Fig. 2) is an approximation but the same profile applies for every year regardless of exact meteorological or traffic congestion conditions, which may vary. Moreover, our results indicate consistently (but not always significantly) higher emissions than the inventories, and while it is difficult to extrapolate these to a yearly total, the idea that NO_x emissions from road transport may still be underestimated is widespread. To minimise the uncertainties in the emission estimates from car MAX-DOAS, more measurements are needed, which should not only cover different seasons but also different times of the day. These measurements should in particular follow the guidelines elaborated in this study to select well-suited driving routes and wind conditions to minimise the errors in the derived NO_x emissions. Results of the car MAX-DOAS measurements and model results for all days together with the wind fields are shown in Fig. A9.

Data availability. Data will be made available by the authors on request.

Appendix A

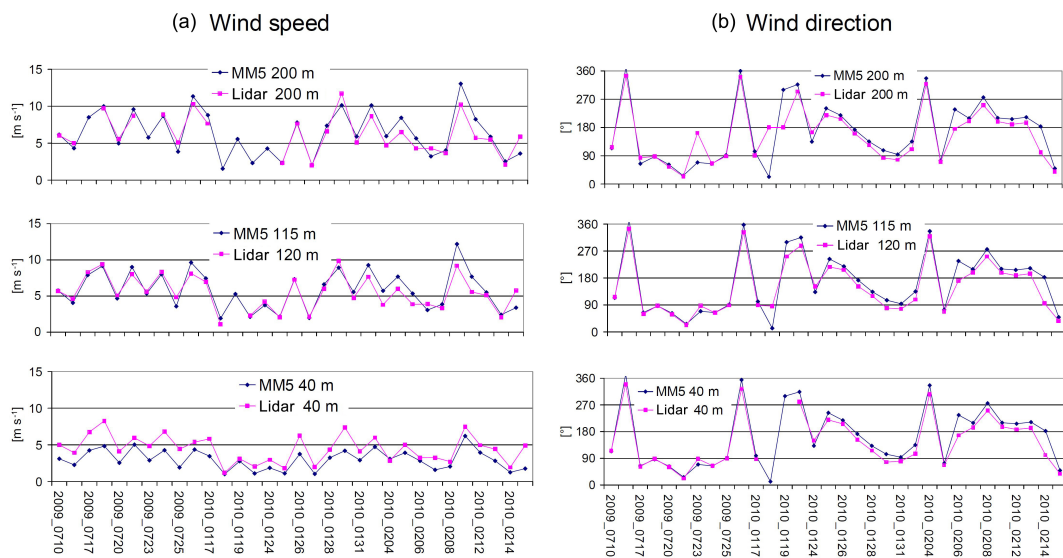


Figure A1. Comparison of the wind fields (**a**: speed; **b**: direction) derived from the MM5 model and the wind lidar at the SIRTA site at Palaiseu in the south-west of Paris for three altitude levels.

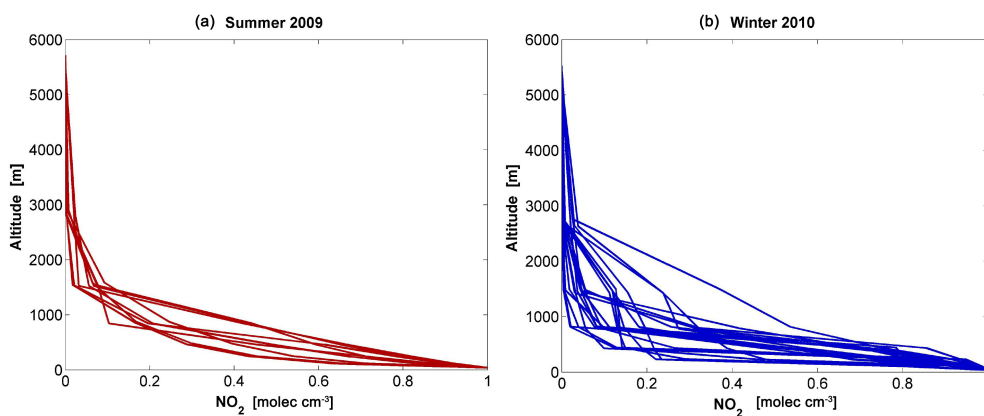


Figure A2. Daily CHIMERE NO₂ profiles (normalised by the surface values) for summer (**a**) and winter (**b**) extracted for the locations where the maximum NO₂ VCDs were measured by car MAX-DOAS.

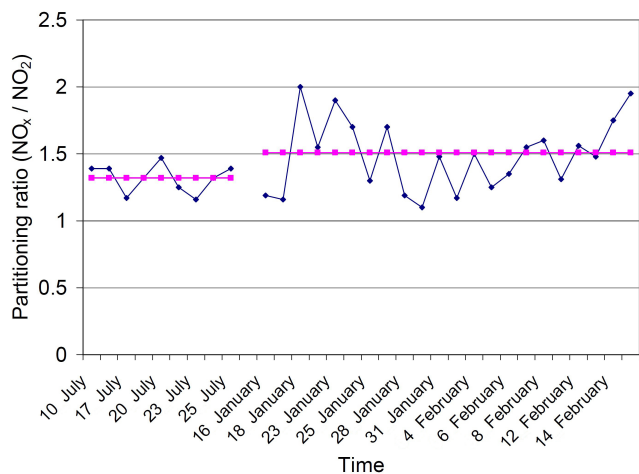


Figure A3. Partitioning ratios derived from the model simulations for the locations of the maximum NO₂ VCDs for all days of the campaigns. A large day-to-day fluctuation but also a systematic difference between winter and summer is found. The average ratios for summer and winter are 1.32 and 1.51, respectively.

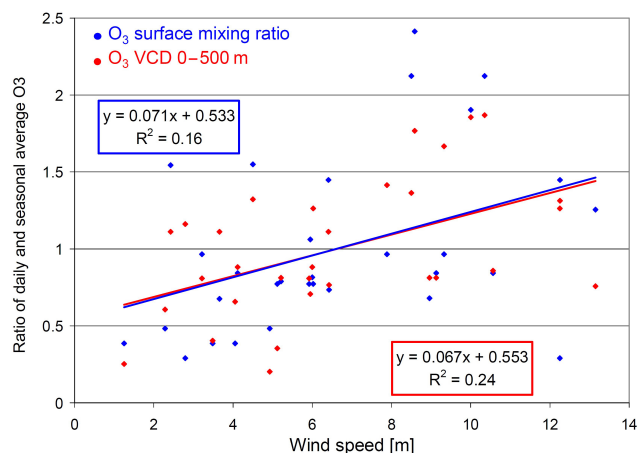


Figure A5. Dependence of the surface mixing ratios and O₃ VCDs on wind speed. To account for the seasonal differences, the daily values are divided by the respective seasonal averages.

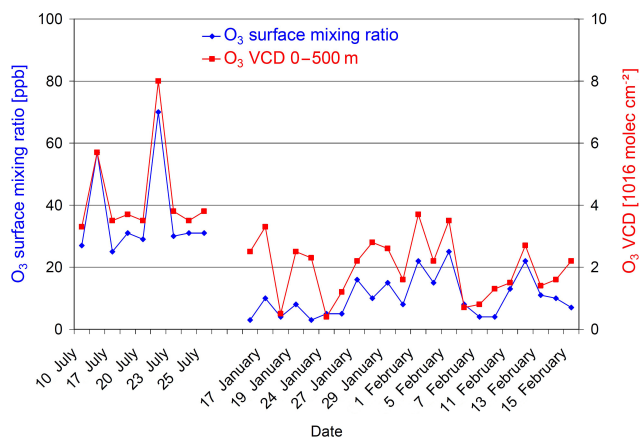


Figure A4. O₃ mixing ratios and tropospheric VCDs at the location of the highest NO₂ VCDs for all days.

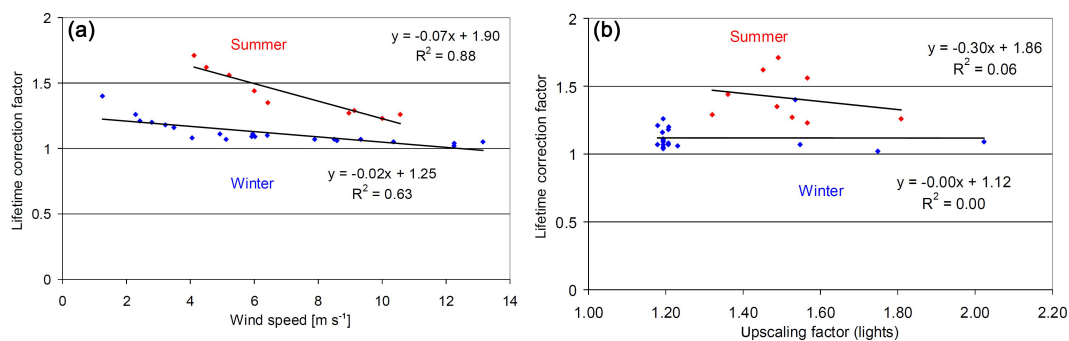


Figure A6. Dependence of the lifetime correction factor on wind speed (a) and the size of the circle (b, represented by the upscaling factor).

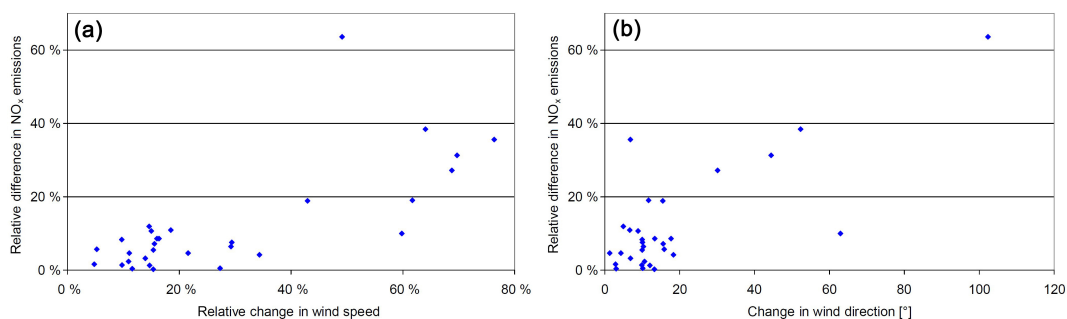


Figure A7. Difference in the NO_x emissions derived with either averaged or variable wind data plotted versus the variability in the wind speed (a) and wind direction (b).

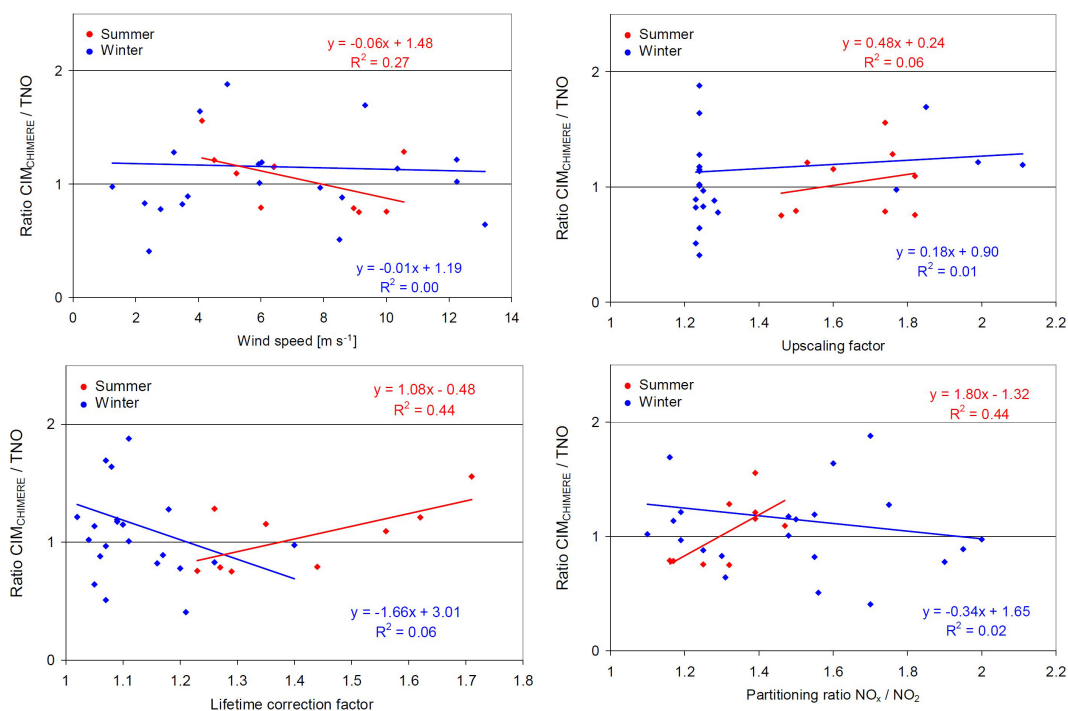


Figure A8. Dependence of the ratio of the derived emissions (CIM_{CHIMERE}) and TNO NO_x emissions on different parameters for summer (red) and winter (blue).

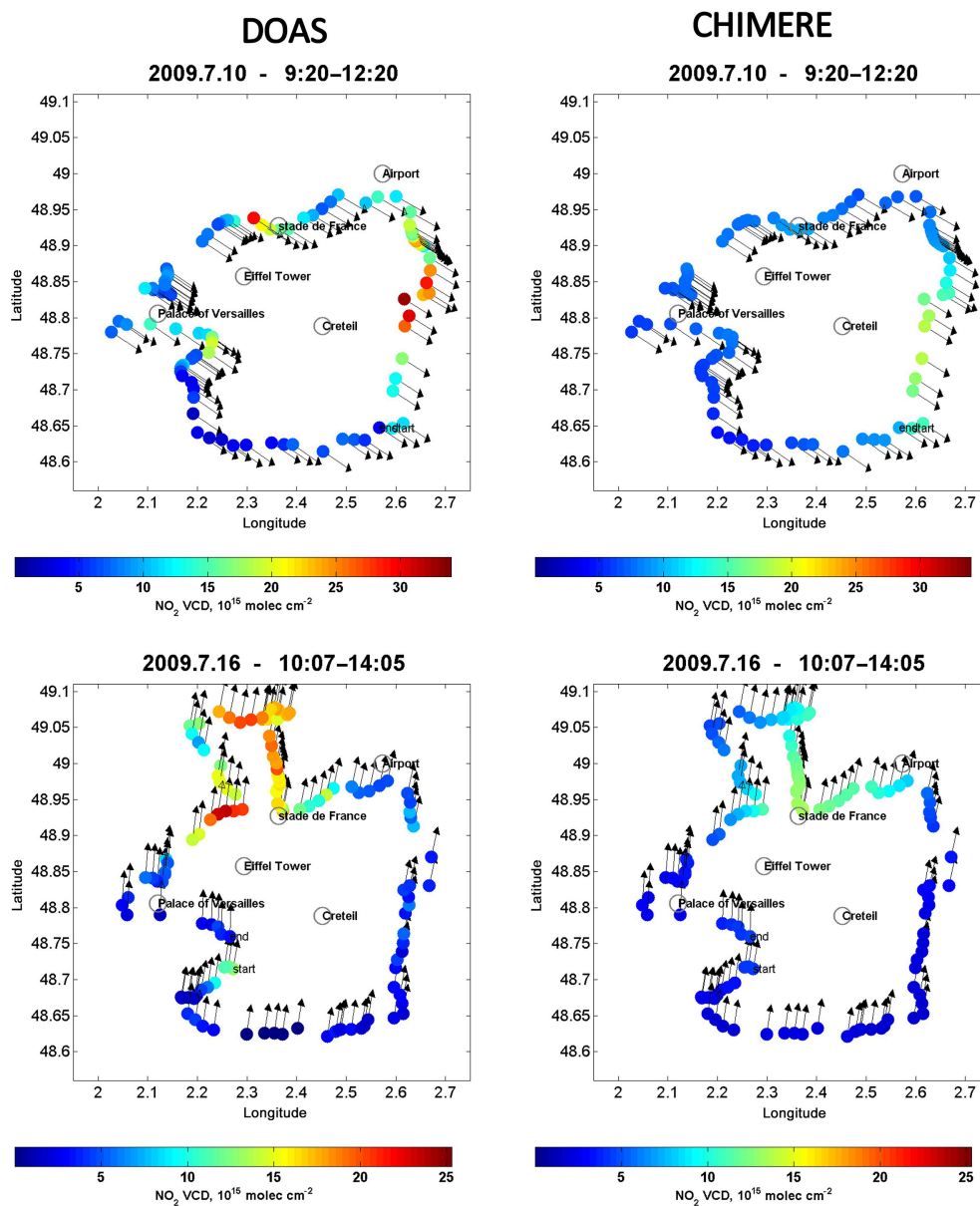


Figure A9.

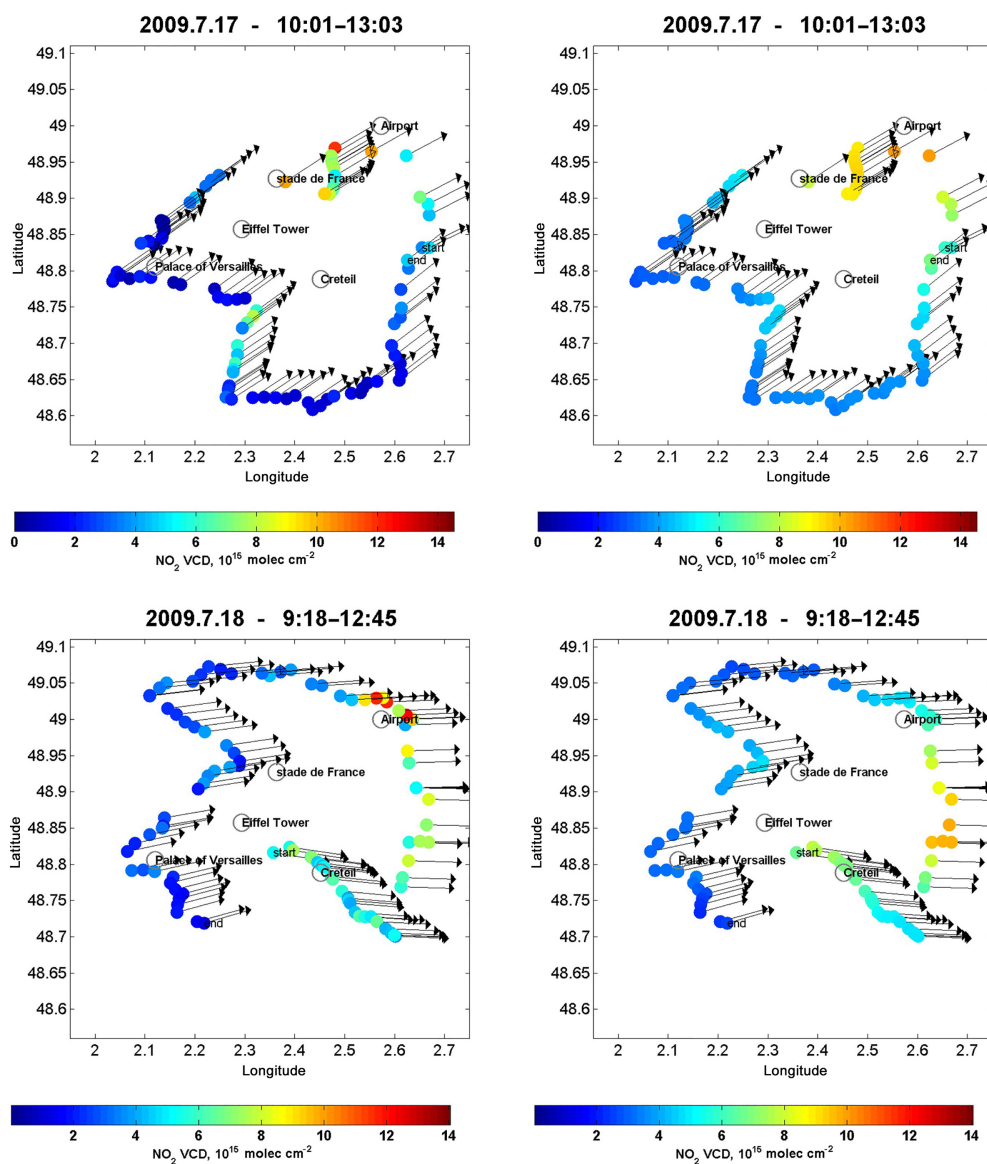


Figure A9.

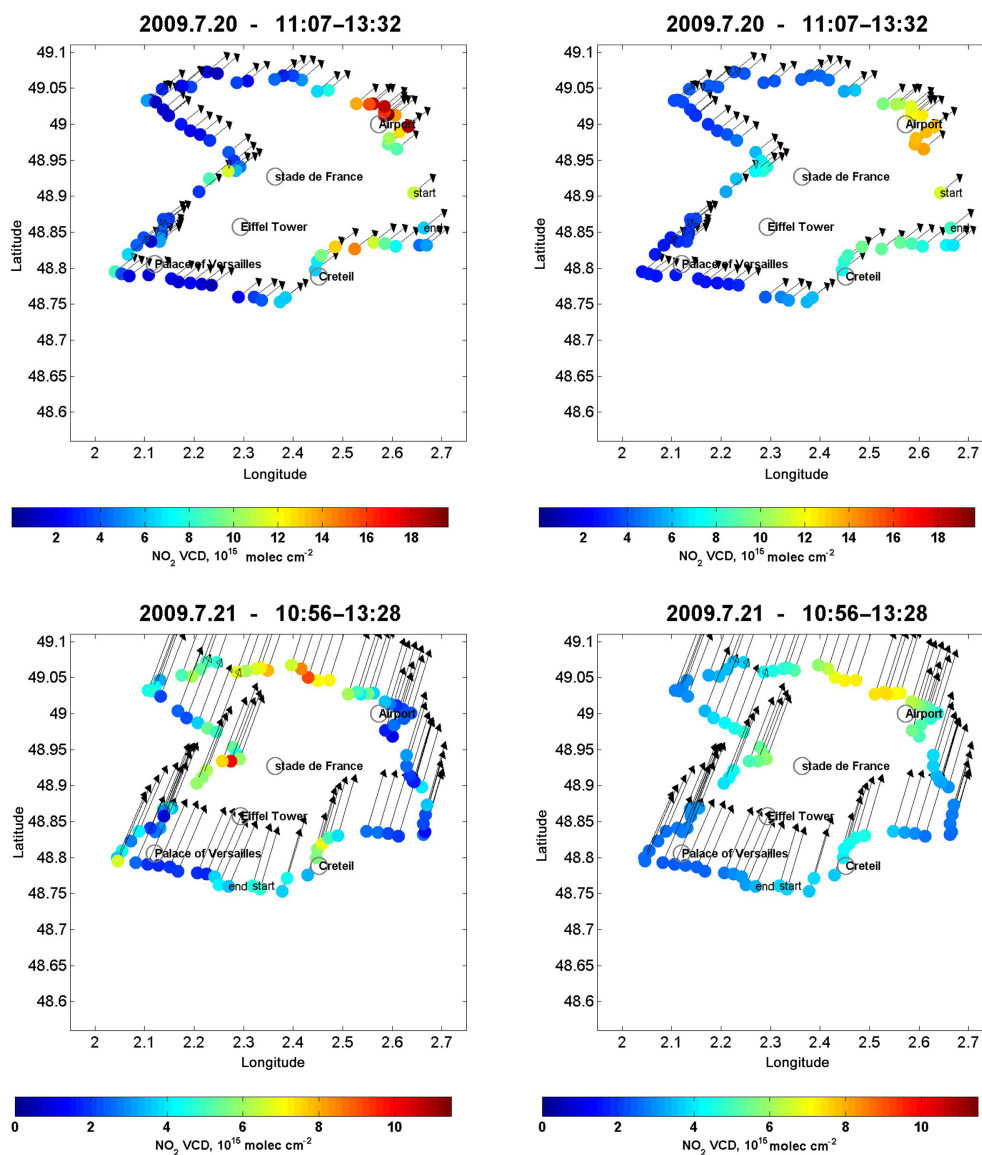


Figure A9.

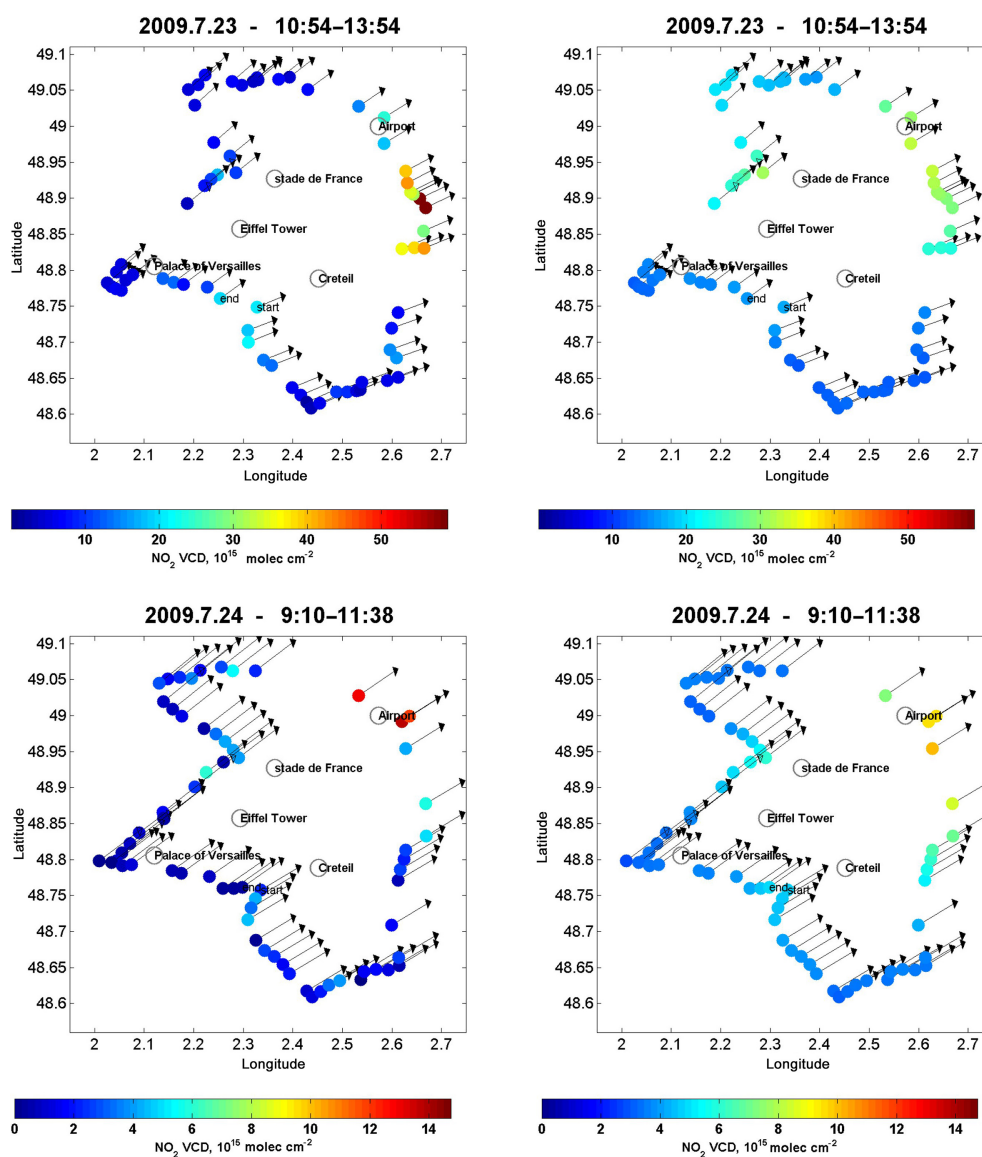


Figure A9.

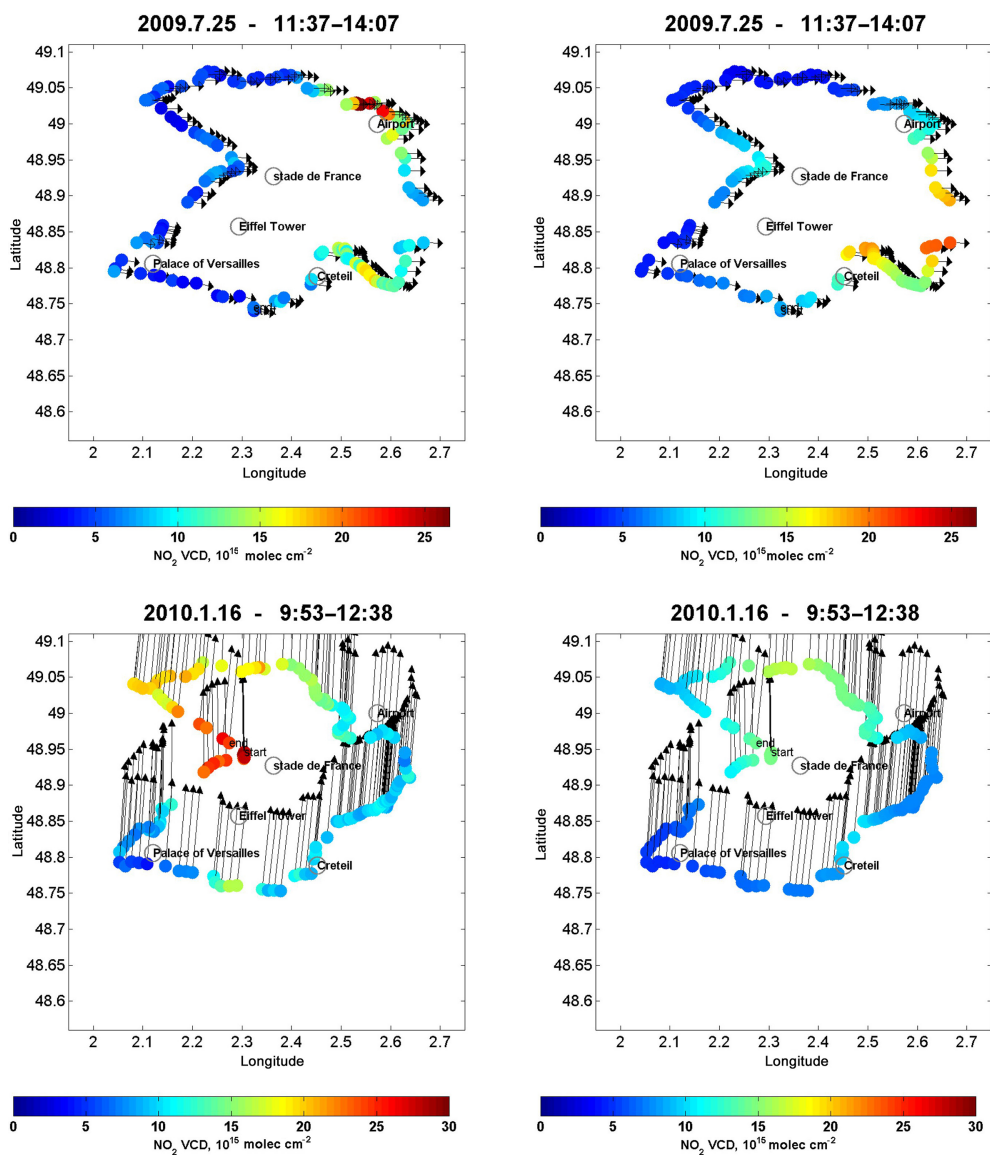


Figure A9.

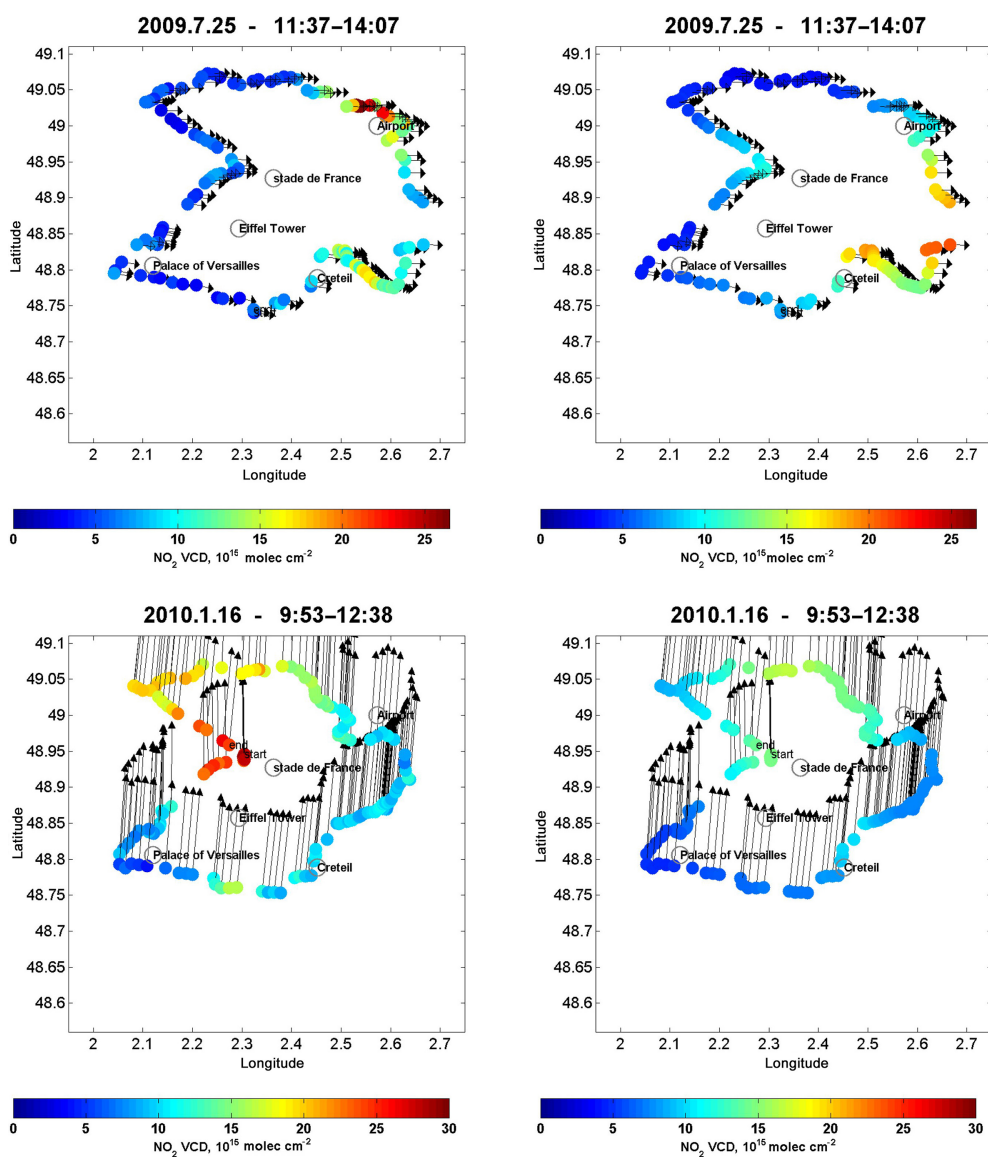


Figure A9.

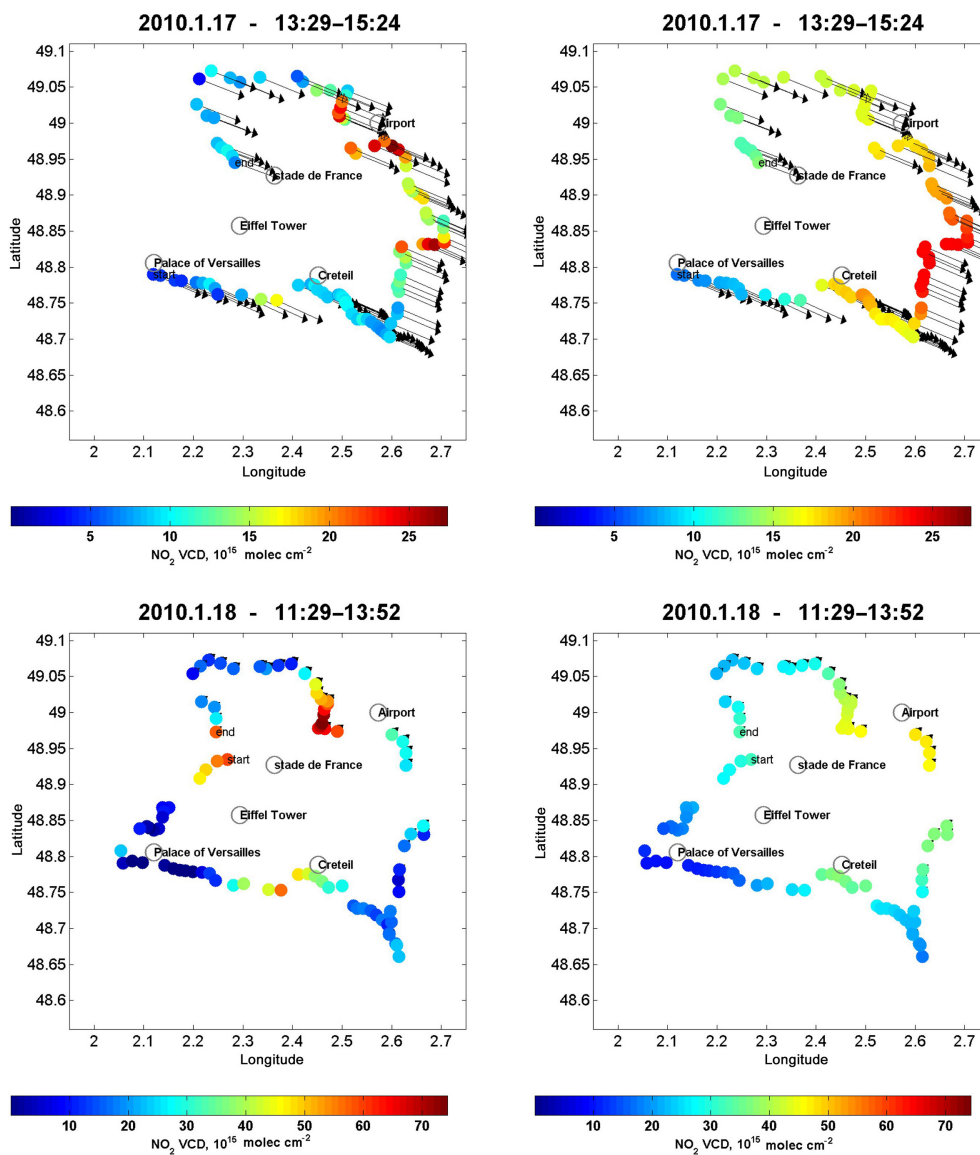


Figure A9.

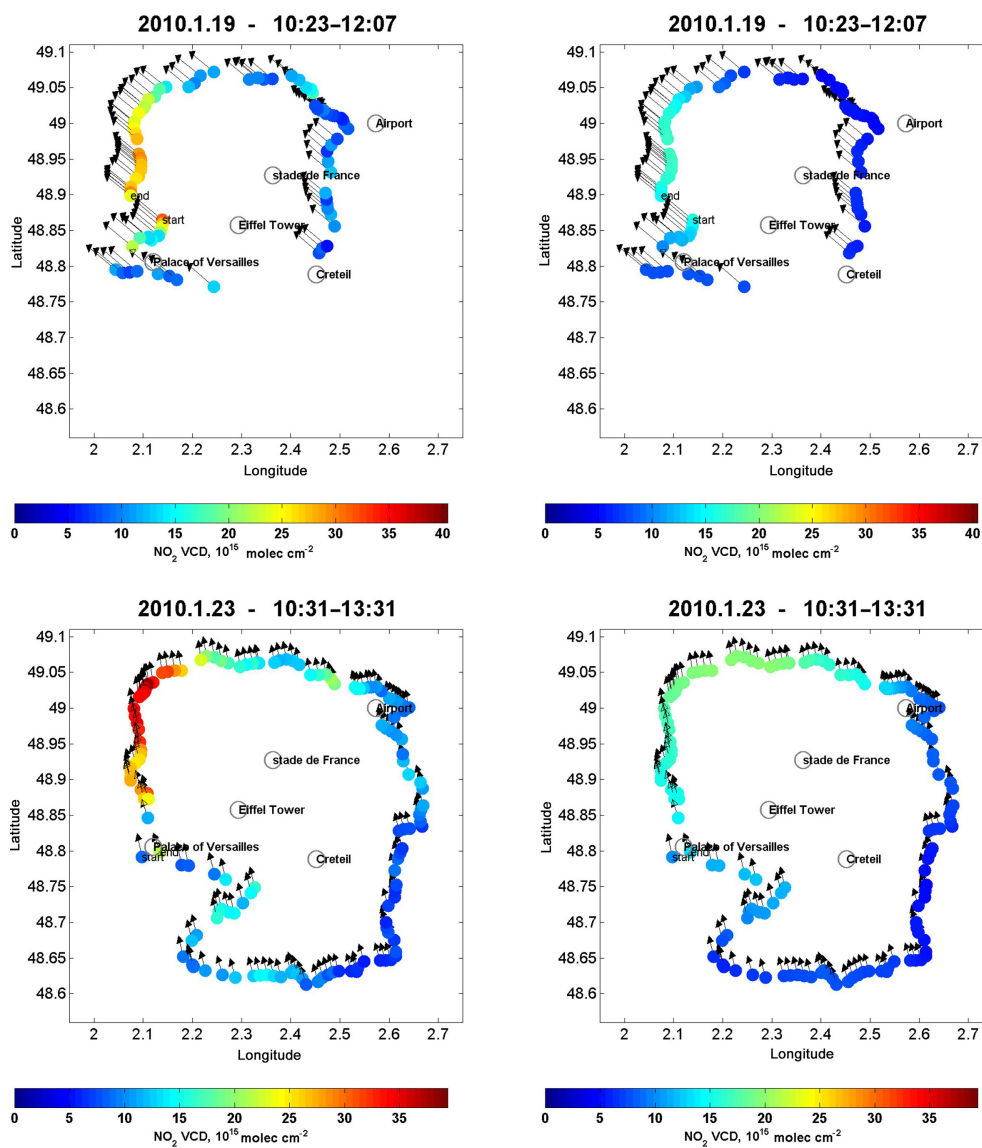
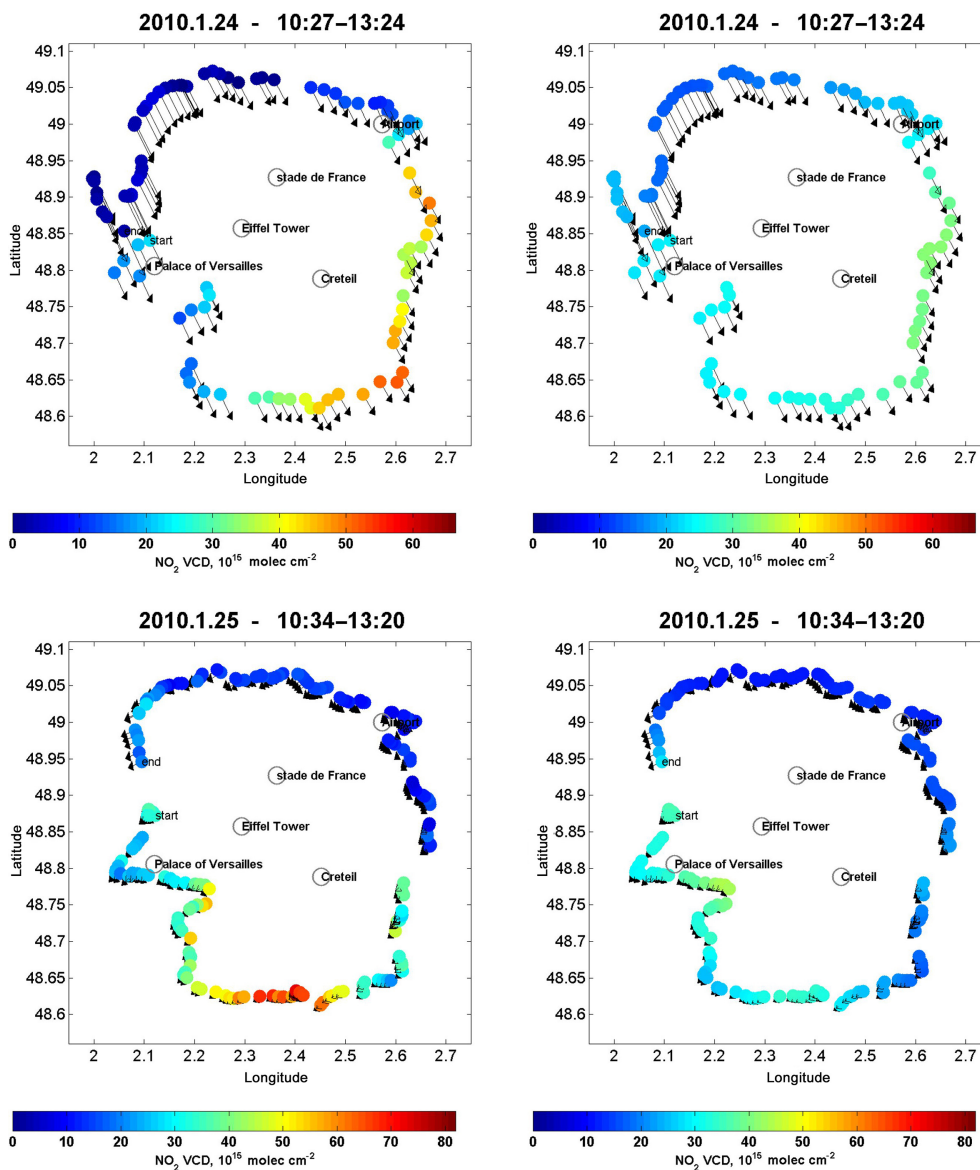
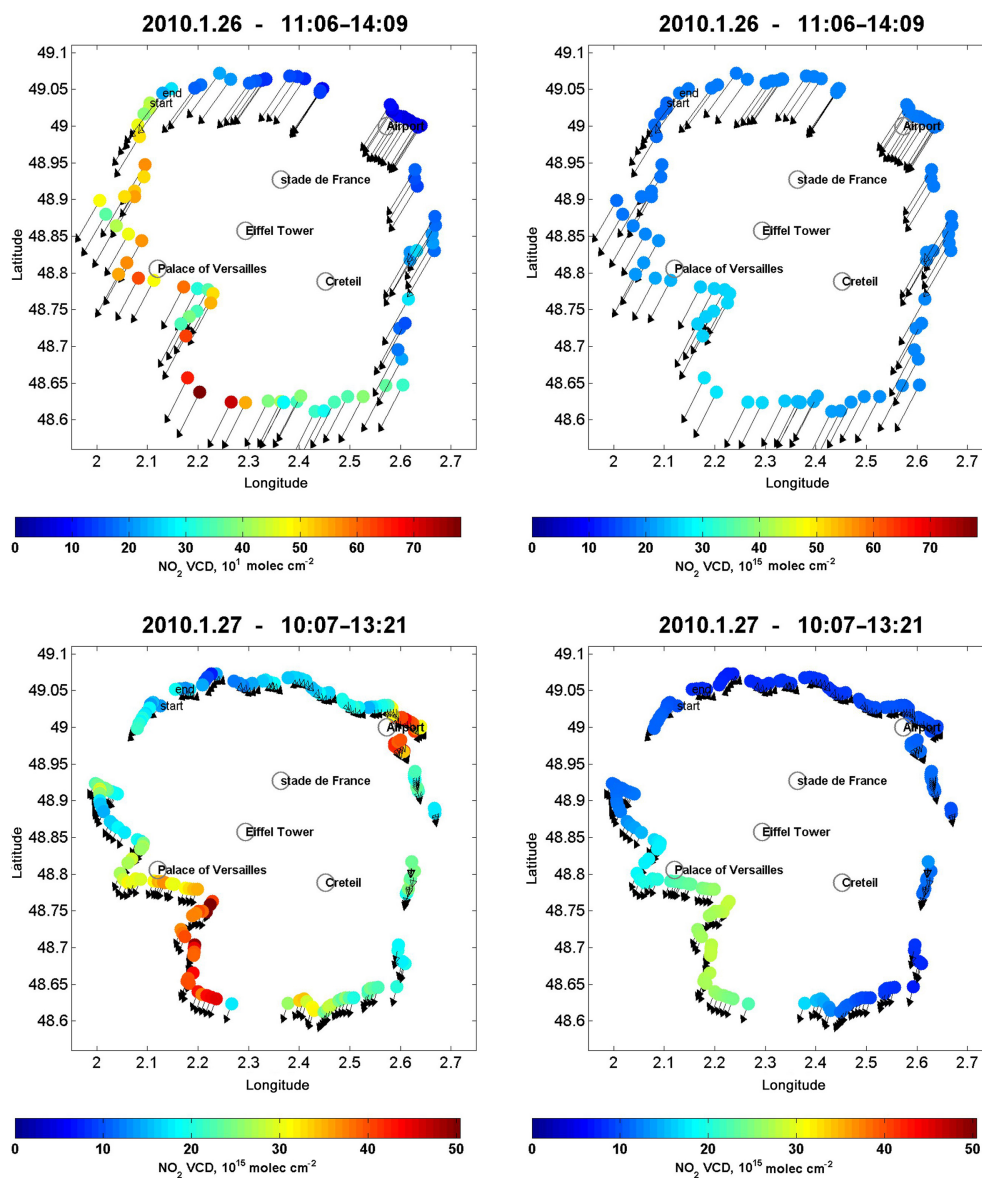
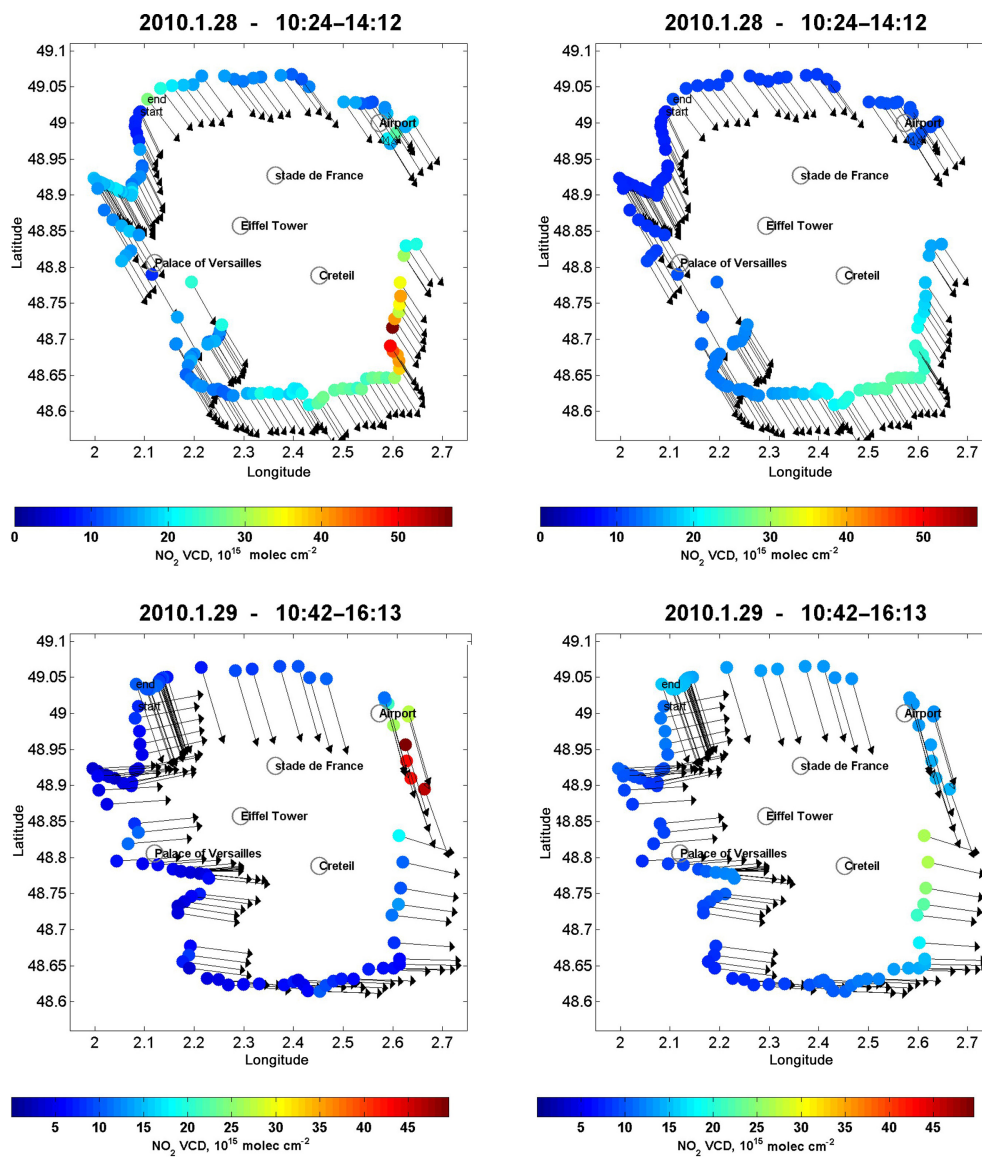
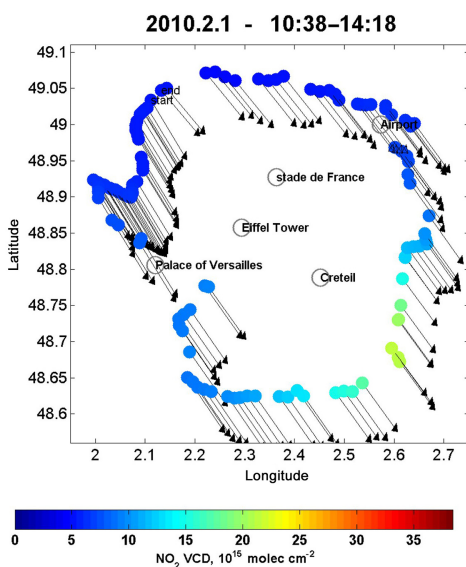
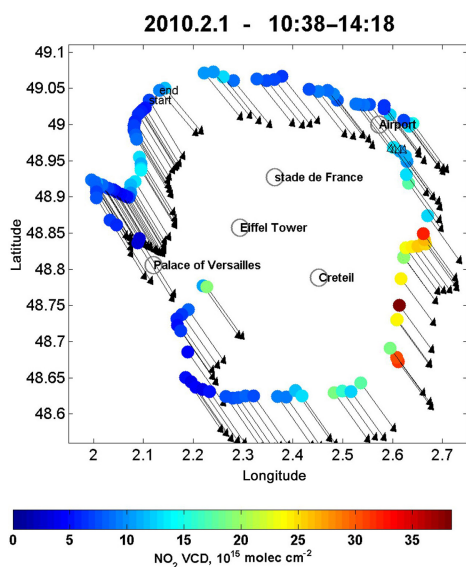
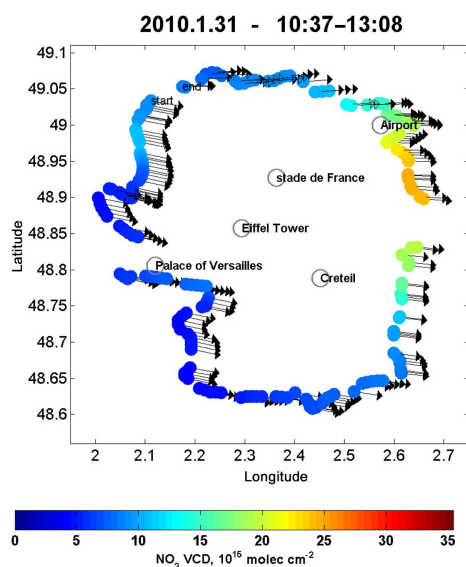
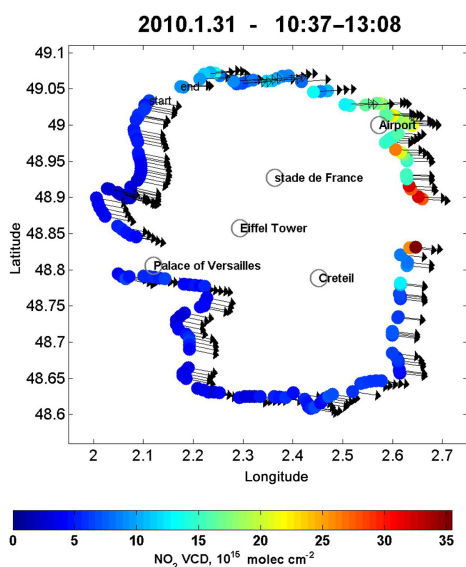


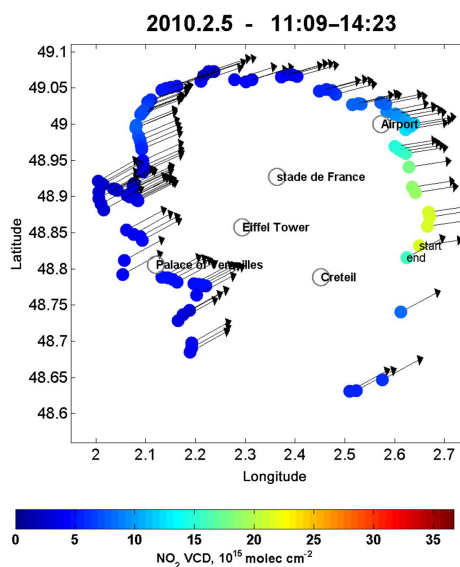
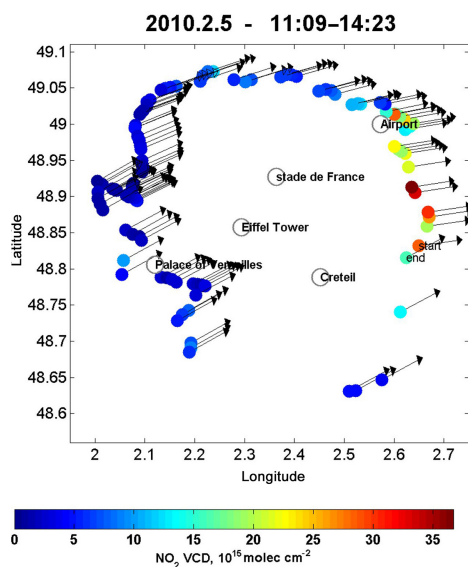
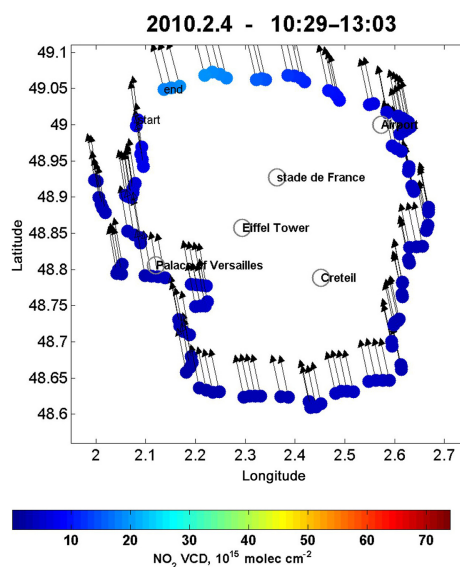
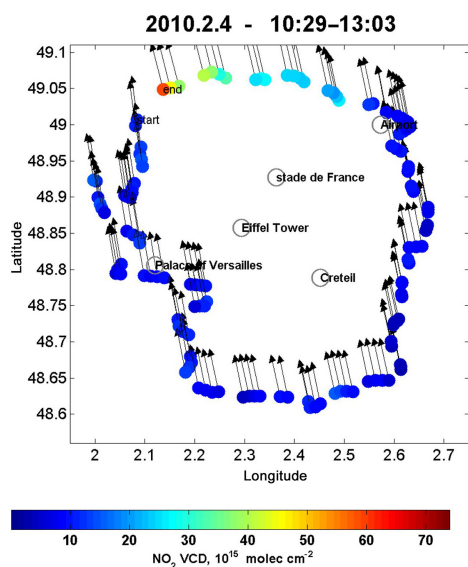
Figure A9.

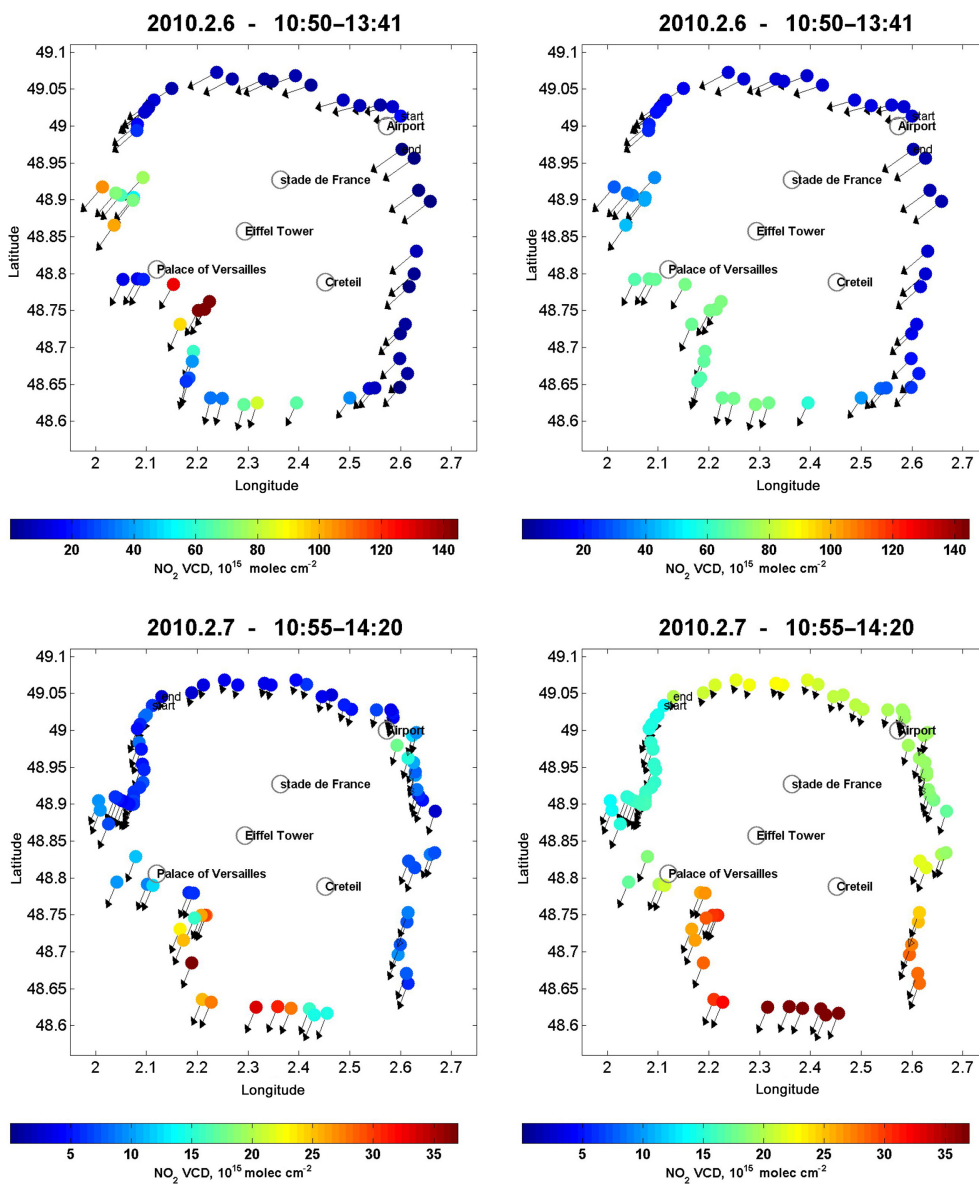


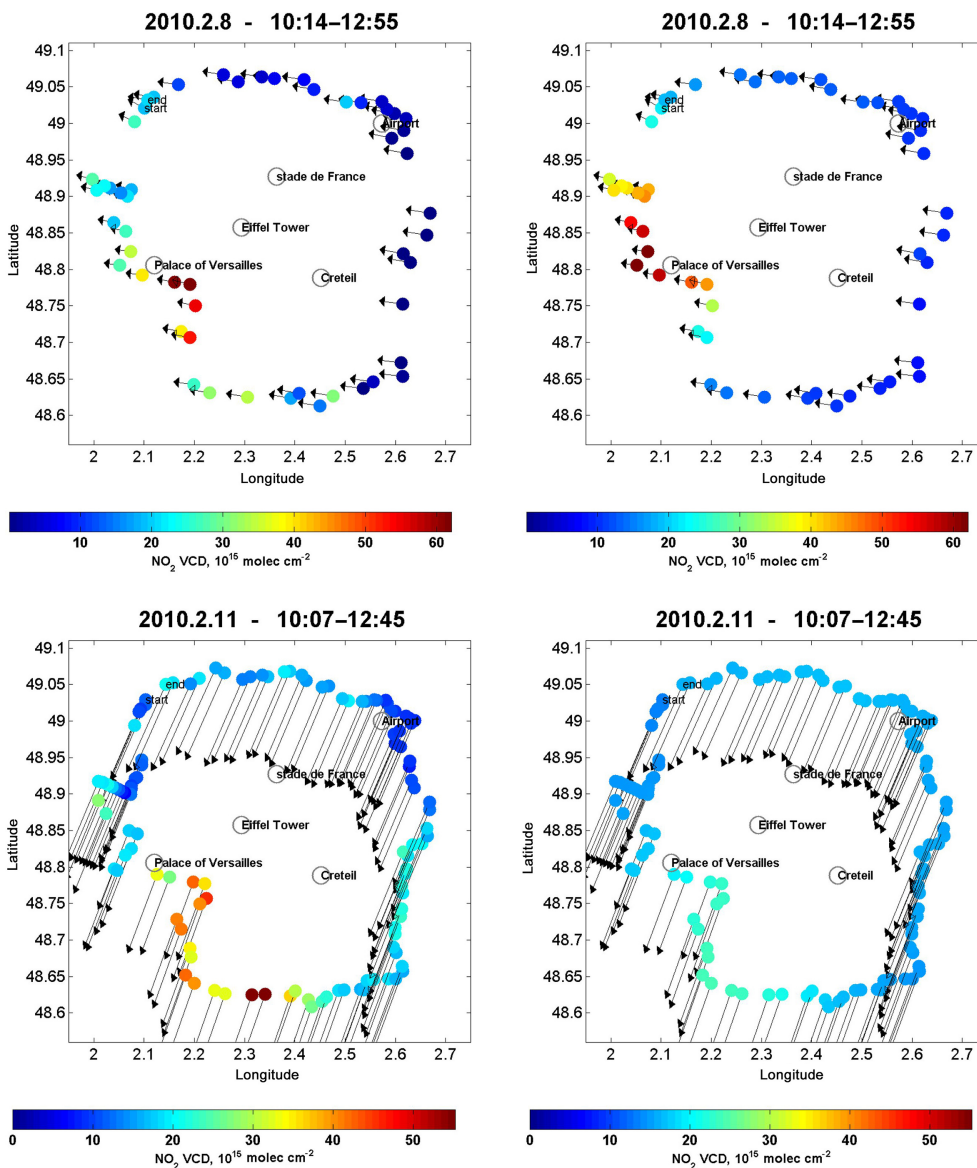


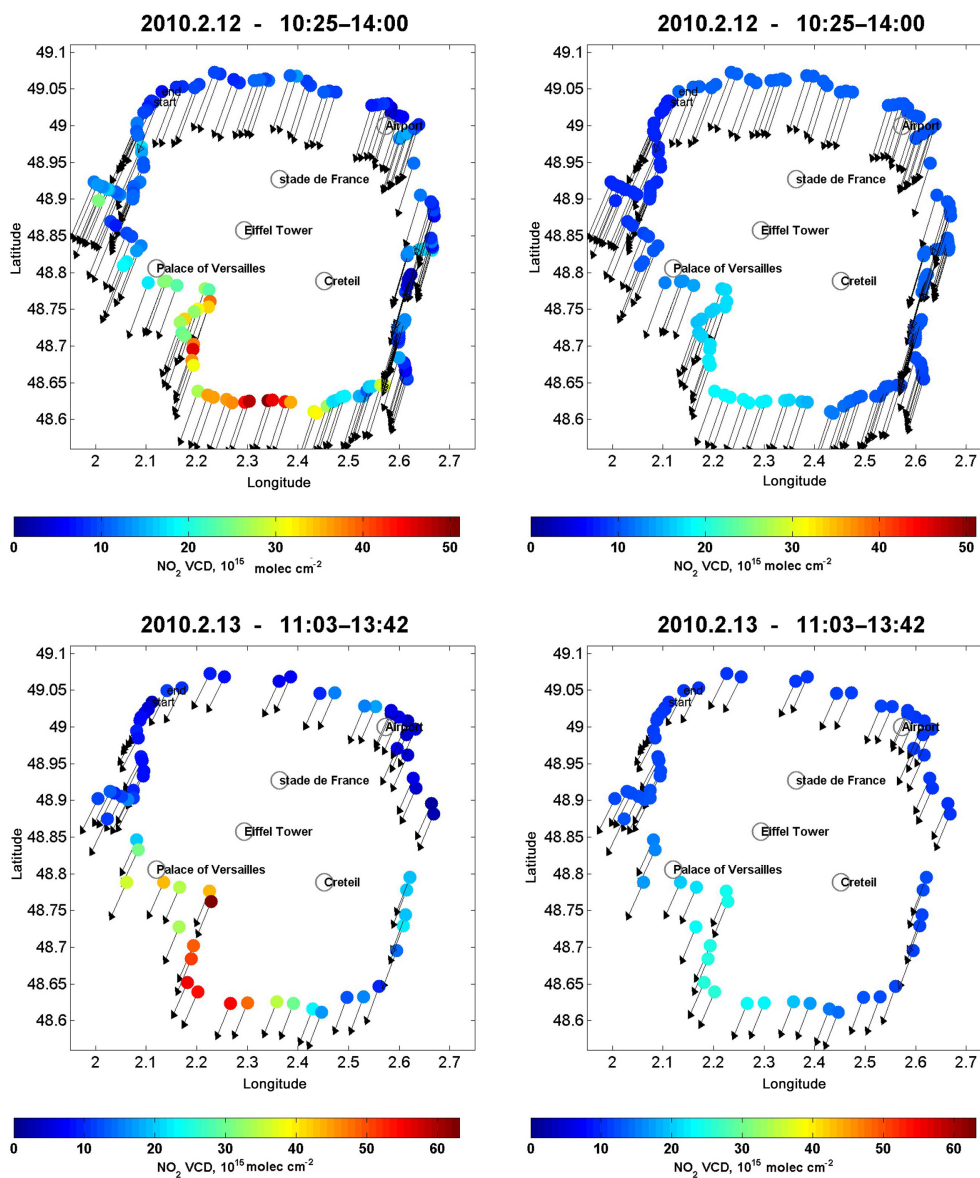












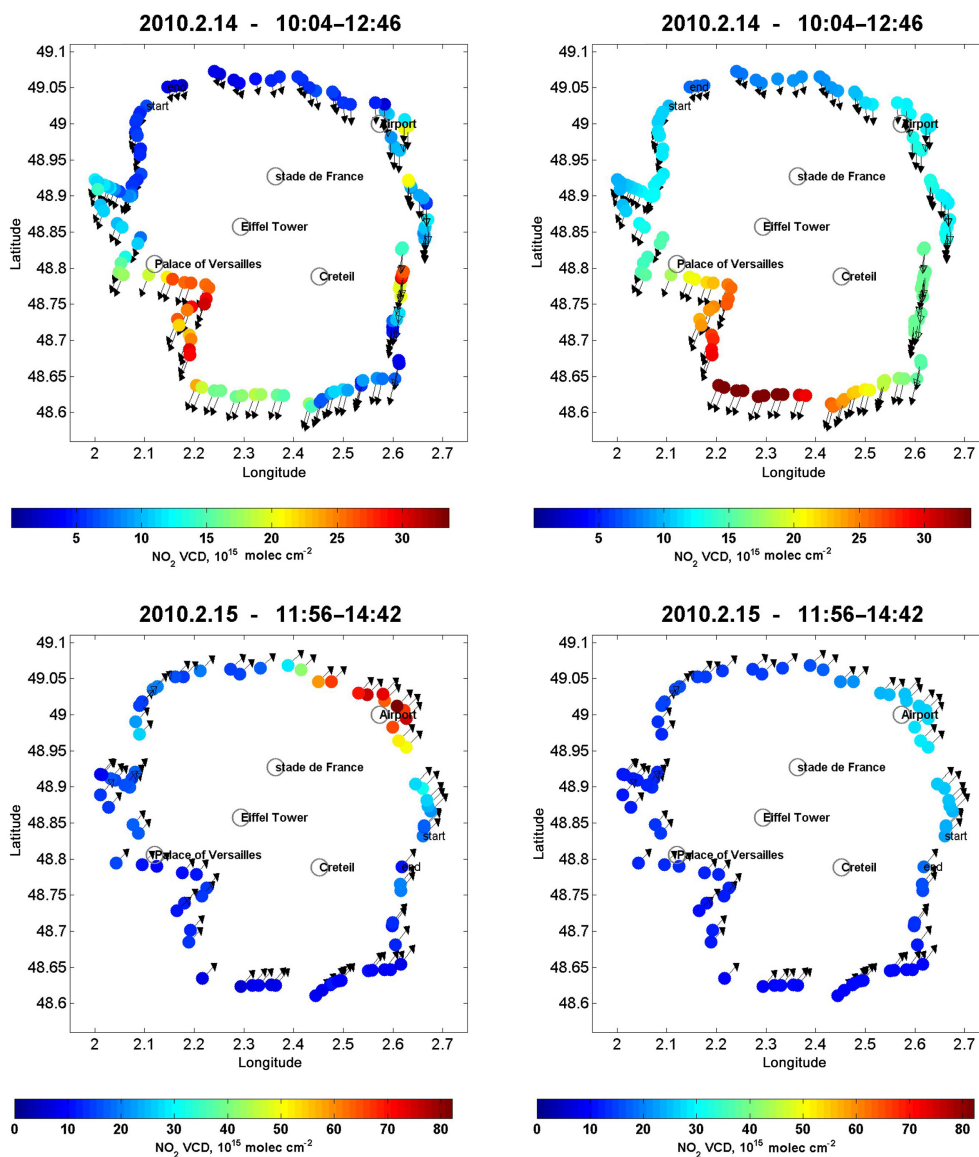


Figure A1. NO_2 VCDs and wind vectors for all days of both campaigns. Left column shows the results of the car MAX-DOAS measurements, and right column shows the corresponding model results. Dates are given as yyyy.m.dd.

Competing interests. The authors declare that they have no conflict of interest.

Acknowledgements. The research leading to these results has received funding from the European Union's Seventh Framework Programme FP/2007-2011 within the project MEGAPOLI, grant agreement no. 212520. We are very thankful to several drivers, who supported the car MAX-DOAS measurements: Thierry Marbach, Tobias Tröndle, Steffen Dörner, Christoph Hörmann, Bastian Jäcker and Sven Krautwurst. The authors would like to acknowledge: Jean-Charles Dupont and the SIRTa team for providing the wind cube lidar data used in this study. We acknowledge Airparif (see <http://www.airparif.asso.fr/en/index/index>) for providing the emission data for the greater Paris region.

The article processing charges for this open-access publication were covered by the Max Planck Society.

Edited by: Robert McLaren

Reviewed by: two anonymous referees

References

- Airparif: Ile-de-France gridded emission inventory 2005 (version 2008), <http://www.airparif.asso.fr/> (last access: 19 June 2017), 2010.
- Baklanov, A., Lawrence, M., Pandis, S., Mahura, A., Finardi, S., Moussiopoulos, N., Beekmann, M., Laj, P., Gomes, L., Jaffrezo, J.-L., Borbon, A., Coll, I., Gros, V., Sciare, J., Kukkonen, J., Galmari, S., Giorgi, F., Grimmond, S., Esau, I., Stohl, A., Denby, B., Wagner, T., Butler, T., Baltensperger, U., Builtjes, P., van den Hout, D., van der Gon, H. D., Collins, B., Schluenzen, H., Kulmala, M., Zilitinkevich, S., Sokhi, R., Friedrich, R., Theloke, J., Kummer, U., Jalkanen, L., Halenka, T., Wiedensohler, A., Pyle, J., and Rossow, W. B.: MEGAPOLI: concept of multi-scale modelling of megacity impact on air quality and climate, *Adv. Sci. Res.*, 4, 115–120, <https://doi.org/10.5194/asr-4-115-2010>, 2010.
- Beekmann, M., Prévôt, A. S. H., Drewnick, F., Sciare, J., Pandis, S. N., Denier van der Gon, H. A. C., Crippa, M., Freutel, F., Poulain, L., Ghersi, V., Rodriguez, E., Beirle, S., Zotter, P., von der Weiden-Reinmüller, S.-L., Bressi, M., Fountoukis, C., Petetin, H., Szidat, S., Schneider, J., Rosso, A., El Haddad, I., Megaritis, A., Zhang, Q. J., Michoud, V., Slowik, J. G., Moukhtar, S., Kolmonen, P., Stohl, A., Eckhardt, S., Borbon, A., Gros, V., Marchand, N., Jaffrezo, J. L., Schwarzenboeck, A., Colomb, A., Wiedensohler, A., Borrmann, S., Lawrence, M., Baklanov, A., and Baltensperger, U.: In situ, satellite measurement and model evidence on the dominant regional contribution to fine particulate matter levels in the Paris megacity, *Atmos. Chem. Phys.*, 15, 9577–9591, <https://doi.org/10.5194/acp-15-9577-2015>, 2015.
- Beirle, S., Boersma, F., Platt, U., Lawrence, M. G., and Wagner, T.: Megacity emissions and lifetimes of nitrogen oxides probes from space, *Science*, 333, 1737–1739, <https://doi.org/10.1126/science.1207824>, 2011.
- Denier van der Gon, H. A. C., Beevers, S., D'Allura, A., Finardi, S., Honoré, C., Kuenen, J., Perrussel, O., Radice, P., Theloke, J., Uzbisich, M., and Visschedijk, A.: Discrepancies Between Top-Down and Bottom-Up Emission Inventories of Megacities: The Causes and Relevance for Modeling Concentrations and Exposure, in: *Air Pollution Modeling and its Application XXI*, NATO Science for Peace and Security Series C: Environmental Security, edited by: Steyn D. and Trini Castelli, S., Springer, Dordrecht, 2011.
- Dudhia, A., Smith, S. E., Wood, A. R., and Taylor, F. W.: Diurnal and semi-diurnal temperature variability of the middle atmosphere, as observed by ISAMS, *Geophys. Res. Lett.*, 20, 1251–1254, <https://doi.org/10.1029/93GL01107>, 1993.
- Ghude, S. D., Pfister, G. G., Jena, C., van der A, R. J., Emmons, L. K., and Kumar, R.: Satellite constraints of nitrogen oxide (NO_x) emissions from India based on OMI observations and WRF-Chem simulations, *Geophys. Res. Lett.*, 1, 423–428, <https://doi.org/10.1029/2012GL053926>, 2013.
- Haefelin, M., Barthès, L., Bock, O., Boitel, C., Bony, S., Bouniol, D., Chepfer, H., Chiriac, M., Cuesta, J., Delanoë, J., Drobinski, P., Dufresne, J.-L., Flamant, C., Grall, M., Hodzic, A., Hourdin, F., Lapouge, F., Lemaître, Y., Mathieu, A., Morille, Y., Naud, C., Noël, V., O'Hirok, W., Pelon, J., Pietras, C., Protat, A., Romand, B., Scialom, G., and Vautard, R.: SIRTa, a ground-based atmospheric observatory for cloud and aerosol research, *Ann. Geophys.*, 23, 253–275, <https://doi.org/10.5194/angeo-23-253-2005>, 2005.
- Ibrahim, O., Shaiganfar, R., Sinreich, R., Stein, T., Platt, U., and Wagner, T.: Car MAX-DOAS measurements around entire cities: quantification of NO_x emissions from the cities of Mannheim and Ludwigshafen (Germany), *Atmos. Meas. Tech.*, 3, 709–721, <https://doi.org/10.5194/amt-3-709-2010>, 2010.
- Menut, L., Goussebaile, A., Bessagnet, B., Khvorostyanov, K., and Ung, A.: Impact of realistic hourly emissions profiles on air pollutants concentrations modelled with CHIMERE, *Atmos. Environ.*, 49, 233–244, <https://doi.org/10.1016/j.atmosenv.2011.11.057>, 2012.
- Menut, L., Bessagnet, B., Khvorostyanov, D., Beekmann, M., Blond, N., Colette, A., Coll, I., Curci, G., Foret, G., Hodzic, A., Mailler, S., Meleux, F., Monge, J.-L., Pison, I., Siour, G., Turquety, S., Valari, M., Vautard, R., and Vivanco, M. G.: CHIMERE 2013: a model for regional atmospheric composition modelling, *Geosci. Model Dev.*, 6, 981–1028, doi:10.5194/gmd-6-981-2013, 2013.
- Petetin, H., Beekmann, M., Colomb, A., Denier van der Gon, H. A. C., Dupont, J.-C., Honoré, C., Michoud, V., Morille, Y., Perrussel, O., Schwarzenboeck, A., Sciare, J., Wiedensohler, A., and Zhang, Q. J.: Evaluating BC and NO_x emission inventories for the Paris region from MEGAPOLI aircraft measurements, *Atmos. Chem. Phys.*, 15, 9799–9818, <https://doi.org/10.5194/acp-15-9799-2015>, 2015.
- Rivera, C., Sosa, G., Wöhrnschimmel, H., de Foy, B., Johansson, M., and Galle, B.: Tula industrial complex (Mexico) emissions of SO₂ and NO₂ during the MCMA 2006 field campaign using a mobile mini-DOAS system, *Atmos. Chem. Phys.*, 9, 6351–6361, <https://doi.org/10.5194/acp-9-6351-2009>, 2009.
- Seinfeld, J. H. and Pandis, S. N.: *Atmospheric Chemistry and Physics: From Air Pollution to Climate Change*, chap. 6.5, John Wiley & Sons, Hoboken, 2012.
- Schmidt, H., Derognat, C., Vautard, R., and Beekmann, M.: A comparison of simulated and observed ozone mixing ratios for the

- summer of 1998 in western Europe, *Atmos. Environ.*, **35**, 6277–6297, 2001.
- Shaiganfar, R., Beirle, S., Sharma, M., Chauhan, A., Singh, R. P., and Wagner, T.: Estimation of NO_x emissions from Delhi using Car MAX-DOAS observations and comparison with OMI satellite data, *Atmos. Chem. Phys.*, **11**, 10871–10887, <https://doi.org/10.5194/acp-11-10871-2011>, 2011.
- Shaiganfar, R., Beirle, S., Petetin, H., Zhang, Q., Beekmann, M., and Wagner, T.: New concepts for the comparison of tropospheric NO₂ column densities derived from car-MAX-DOAS observations, OMI satellite observations and the regional model CHIMERE during two MEGAPOLI campaigns in Paris 2009/10, *Atmos. Meas. Tech.*, **8**, 2827–2852, <https://doi.org/10.5194/amt-8-2827-2015>, 2015.
- Terrenoire, E., Bessagnet, B., Rouïl, L., Tognet, F., Pirovano, G., Létinois, L., Beauchamp, M., Colette, A., Thunis, P., Amann, M., and Menut, L.: High-resolution air quality simulation over Europe with the chemistry transport model CHIMERE, *Geosci. Model Dev.*, **8**, 21–42, <https://doi.org/10.5194/gmd-8-21-2015>, 2015.
- Timmermans, R. M. A., Denier van der Gon, H. A. C., Kuenen, J. J. P., Segers, A. J., Honoré, C., Perrussel, O., Builtjes, P. J. H., and Schaap, M.: Quantification of the urban air pollution increment and its dependency on the use of down-scaled and bottom-up city emission inventories, *Urban Climate*, **6**, 46–62, 2013.
- Wagner, T., Ibrahim, O., Shaiganfar, R., and Platt, U.: Mobile MAX-DOAS observations of tropospheric trace gases, *Atmos. Meas. Tech.*, **3**, 129–140, <https://doi.org/10.5194/amt-3-129-2010>, 2010.
- Ziskin, D., Kimberly, B., Feng, C. H., Tilottama, G., and Chris, E.: Methods Used For the 2006 Radiance Lights, Proceedings of the 30th Asia-Pacific Advanced Network Meeting, 131–142, <http://journals.sfu.ca/apan/index.php/apan/article/view/88> (last access: 19 June 2017), 2010.
- Zhang, Q. J., Beekmann, M., Drewnick, F., Freutel, F., Schneider, J., Crippa, M., Prevot, A. S. H., Baltensperger, U., Poulain, L., Wiedensohler, A., Sciare, J., Gros, V., Borbon, A., Colomb, A., Michoud, V., Doussin, J.-F., Denier van der Gon, H. A. C., Haeffelin, M., Dupont, J.-C., Siour, G., Petetin, H., Bessagnet, B., Pandis, S. N., Hodzic, A., Sanchez, O., Honoré, C., and Perrussel, O.: Formation of organic aerosol in the Paris region during the MEGAPOLI summer campaign: evaluation of the volatility-basis-set approach within the CHIMERE model, *Atmos. Chem. Phys.*, **13**, 5767–5790, <https://doi.org/10.5194/acp-13-5767-2013>, 2013.
- Zhang, Q. J., Beekmann, M., Freney, E., Sellegri, K., Pichon, J. M., Schwarzenboeck, A., Colomb, A., Bourriane, T., Michoud, V., and Borbon, A.: Formation of secondary organic aerosol in the Paris pollution plume and its impact on surrounding regions, *Atmos. Chem. Phys.*, **15**, 13973–13992, <https://doi.org/10.5194/acp-15-13973-2015>, 2015.